The copyright of this thesis vests in the author. No quotation from it or information derived from it is to be published without full acknowledgement of the source. The thesis is to be used for private study or non-commercial research purposes only.

Published by the University of Cape Town (UCT) in terms of the non-exclusive license granted to UCT by the author.

University of Cape Town

Probing Primordial Non-Gaussianity using Large Scale Structure

University of Cape Town

by

Yabebal Fantaye

A thesis submitted in partial fulfillment for the degree of Masters in Cosmology

in the
Faculty of Science
Departement of Mathematics
University of Cape Town

November 2009

Thesis directed by

Supervisor: Prof. Bruce Bassett
University of Cape Town/SAAO
South Africa

Co-Supervisor: Dr. Chris Blake
Swinburne University
Australia

and approved by

Internal Examiner:
(University)

External Examiner:
(University)

University of Cape Town

Declaration of Authorship

I declare that this thesis is my own work, and hereby certify that unless stated, all work contained within this thesis is my own to the best of my knowledge.

This thesis is being submitted for the degree of Masters in Cosmology in the department of Mathematics at the University of Cape Town.

Yabebal Tadesse Fantaye
November 2009

University of Cape Town

Abstract

Recent evidence from the WMAP satellite has lead to a tentative detection of non-Gaussianity. Using the bispectrum statistic applied to the MegaZ catalogue of over 600,000 luminous red galaxies we find new bounds on the large-scale non-Gaussianity. We constrain the f_{NL} parameter using a particular type of triangular configuration as well as the combination of all the possible triangles in harmonic space. The constraint on f_{NL} from the combination of all possible triangular configurations is $f_{NL}^{local} = 57 \pm 52$ with 68% confidence limit, which is consistent with vanishing primordial non-Gaussianity, although some triangular configurations on their own suggest a non-zero bispectrum which, if confirmed, would have a profound effect on modern cosmology.

University of Cape Town

Acknowledgment

This thesis arose in part out of the discussion the Cape Town observational Cosmology group had with Dr. Chris Blake in one of the Cosmology gateaways at Hermanus on April of 2007. Since then I have worked with a great number of people whose contribution to the research and the making of the thesis deserves special mention. It is a pleasure to convey my gratitude to them all in my humble acknowledgment.

In the first place I would like to express my deep gratitude to Prof Bruce Bassett and Dr. Chris Blake for their supervision, advice, and guidance from the very early stage of this research as well as giving me extraordinary experiences through out the work. Above all and the most needed, they have provided me unflinching encouragement and support in various ways. Their insight and approach for me to handle new problems served me as a constant oasis of ideas and passions in science, which exceptionally inspire and enrich my growth as a student, a researcher and a scientist.

I would like to acknowledge members of the Fisher4cast team, which is lead by Prof. Bruce Bassett, Renee Hlozek and Jacques Kotze for their discussion, advice, and crucial support during the writing of the thesis. I am thankful that in the midst of all their activity, they accepted to be members of the reading committee. In addition, their friendship and collaboration throughout the development of Fisher4Cast was a great opportunity for me to learn team work and scientific collaboration. Thank you very much guys.

Many thanks for the UCT Observational Cosmology group for their insightful basic-to-advanced Cosmology discussions at the weekly group meetings. I have greatly benefited from these discussions.

University of Cape Town

I greatfully thank Cris Sabiu at the Institute of Cosmology and Gravity (ICG) for his help on running GADGET and GRACOS n-body simulations. He has given me his undivided support at all times I needed.

I would like to thank Prof. Jochen Weller, who invited me at the University College London to present my work, and Prof. Benjamin Wandelt for useful discussions and suggestions on non-Gaussianity in the STIAS meeting.

My family in Ethiopia deserves a special thanks for their continual encouragement and support throughout the thesis. With out their advice and support all this work would not be possible.

Finally I would like to thank the Thabo Mbeki scholarship, the NRF, the Royal Society, SAAO and Swimburne University for financial assistance for my studies and travels.

University of Cape Town

Contents

University of Cape Town

University of Cape Town

List of Figures

University of Cape Town

University of Cape Town

List of Tables

University of Cape Town

Abbreviations

ANN	**A**rtificial **N**eural **N**etworks
BAO	**B**aryon **A**coustic **O**scillation
CL	**C**onfidence **L**imit
CMB	**C**osmic **M**Microwave **B**ackground
COBE	**CO**smic **B**ackground **E**xplorer
DE	**D**ark **E**nergy
FLRW	**F**riedmann-**L**emaître-**R**obertson-**W**alker
GR	**G**eneral **R**elativity
LPT	**L**inear **P**erturbation **T**heory
2OPT	**S**econd **O**rder **P**erturbation **E**quations
LRG	**L**uminous **R**ed **G**alaxies
SDSS	**S**loan **D**igital **S**ky **S**urvey
2SLAQ	**2**dF-SDSS **L**RG **A**nd **Q**SO survey
WMAP	**W**ilkinson **M**icrowave **A**nisotropy **P**robe

Cosmological Parameters

ρ_c	critical density of the Universe
Ω_b	fractional density of baryons today
Ω_{DE}	fractional density of dark energy today
Ω_k	fractional density of curvature today
Ω_m	fractional density of matter today

University of Cape Town

Dedicated to my Parents

University of Cape Town

Chapter 1

Introduction

In this first introductory chapter we present a literature review of some of the basic cosmological topics that are related directly or indirectly to the main topic of this thesis.

1.1 General Relativity

Spacetime is defined as a manifold of events with three dimensions of space and one dimension of time. Co-ordinate distances in a manifold are converted to proper distances by the use of a *metric* which is a fundamental quantity in General Relativity. For instance a spatially flat Lorentzian space time is described by a Minkowski metric :

$$\eta_{\alpha\beta} = \begin{pmatrix} -1 & 0 & 0 & 0 \\ 0 & 1 & 0 & 0 \\ 0 & 0 & 1 & 0 \\ 0 & 0 & 0 & 1 \end{pmatrix} . \tag{1.1}$$

The infinitesimal distance between two events in this metric is given by

$$\begin{aligned} ds^2 &= \sum_{\alpha,\beta=0}^{3} \eta_{\alpha\beta} dx^\alpha dx^\beta \\ &= -dt^2 + dx^2 + dy^2 + dz^2 , \end{aligned} \tag{1.2}$$

where dx^α is the co-ordinate of an event in spacetime : x^0 the time component, and x^1, x^2, x^3 are the three spatial coordinates. Conventionally we do not write

University of Cape Town

the summation sign and repeated indices - one up and one down - are summed over. Greek indices are implicitly known to run from 0 to 3.

In general the spacetime metric is a function of the coordinates. The usual symbol for the general metric is $g_{\alpha\beta}$. The distance between two infinitesimally separated events A and B in this metric is given by

$$ds^2 = g_{\alpha\beta} dx^\alpha dx^\beta \,. \tag{1.3}$$

The key idea of General Relativity is that the metric incorporates gravity. The motion of bodies in spacetime is governed by the geometry of spacetime. A freely falling test body in spacetime follows a special curve called the *geodesic curve* which gives the shortest distance between two events.

Geodesics are found by extremizing the distance, s, by solving the equation $\delta s = 0$ [1]

$$\frac{d^2 x^\alpha}{d\tau^2} + \Gamma^\alpha_{\beta\gamma} \frac{dx^\beta}{d\tau}\frac{dx^\gamma}{d\tau} = 0 \,. \tag{1.4}$$

Here τ is the proper time along the geodesics and $\Gamma^\alpha_{\beta\gamma}$ is the Christoffel symbol, which is just the covariant derivative of the basis vectors of the co-ordinate system, and is given by [1]

$$\Gamma^\alpha_{\beta\gamma} = \frac{g^{\alpha\mu}}{2}(\partial_\gamma g_{\mu\beta} + \partial_\beta g_{\gamma\mu} - \partial_\mu g_{\beta\gamma}) \,, \tag{1.5}$$

where ∂_β is the usual partial derivative.

Using the Christoffel symbols we can define the Riemann curvature tensor, which encodes all the information about the geometry of the spacetime. It is given by [1]:

$$R^\alpha_{\beta\gamma\delta} = \partial_\gamma \Gamma^\alpha_{\beta\delta} - \partial_\delta \Gamma^\alpha_{\beta\gamma} + \Gamma^\alpha_{\mu\gamma}\Gamma^\mu_{\beta\delta} - \Gamma^\alpha_{\mu\delta}\Gamma^\mu_{\beta\gamma} \,. \tag{1.6}$$

The Ricci tensor and Ricci scalar can be found by performing a single and double contraction of $R^\alpha_{\beta\gamma\delta}$. The trace free part of the Riemann tensor is known as the Weyl tensor.

1.1.1 Bianchi Identities

The Bianchi identities are given by [1]

$$\nabla_\eta R_{\alpha\beta\gamma\delta} + \nabla_\gamma R_{\alpha\beta\delta\eta} + \nabla_\delta R_{\alpha\beta\eta\gamma} = 0 \,. \tag{1.7}$$

University of Cape Town

Contraction of this equation twice yields [1, 2].

$$\nabla_\beta (R^{\alpha\beta} - \frac{1}{2} g^{\alpha\beta} R) = \nabla_\beta G^{\alpha\beta} = 0 \,. \tag{1.8}$$

The Einstein tensor is then defined as :

$$G_{\alpha\beta} = R_{\alpha\beta} - \frac{1}{2} g_{\alpha\beta} R \tag{1.9}$$

1.1.2 Einstein Field Equations

In General Relativity energy and momentum are combined in the energy-momentum tensor, $T_{\alpha\beta}$, as shown in Fig. (1.1). For a fluid T_{00} represents the energy density while T_{ii} is proportional to the pressure of the fluid. The Einstein field equations relate $T_{\alpha\beta}$ to the Einstein tensor

$$G_{\alpha\beta} = R_{\alpha\beta} - \frac{1}{2} g_{\alpha\beta} R = \frac{8\pi G}{c^4} T_{\alpha\beta} \,. \tag{1.10}$$

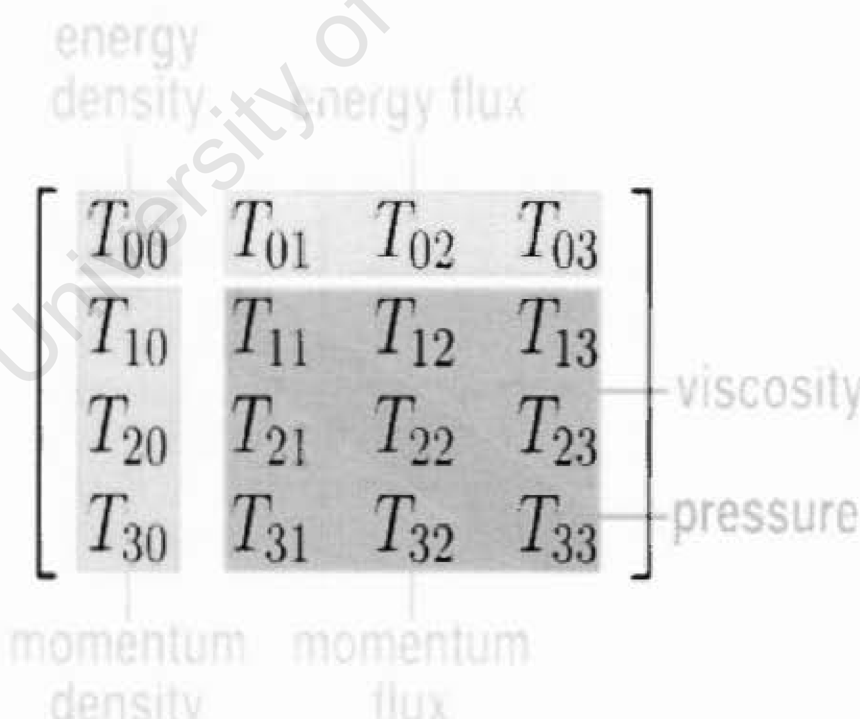

FIGURE 1.1: Components of the energy-momentum tensor. Image made by AugPi. [taken from *www.wikipedia.org*]

University of Cape Town

The meaning of this equation is well illustrated by a saying of J.Wheeler : "spacetime tells matter how to move, matter tells spacetime how to bend". Energy momentum conservation requires $\nabla_\alpha T_{\alpha\beta} = 0$, which follows as the consequence of the Bianchi identity, Eq. (1.7)

1.2 The FLRW Cosmos

A standard assumption in modern Cosmology is that the Universe is homogeneous and isotropic. This assumption is called the *Cosmological principle.* The Universe is said to be homogeneous if the metric is invariant under spatial translations and isotropic if it is invariant under rotations. A space that is isotropic around every point is also homogeneous [3]. However, the reverse is not true, since the Bianchi models for example are homogeneous but anisotropic. Isotropy around one point is also not enough to prove homogeneity. Any spherically symmetric Universe will appear isotropic around the center. Fig. (1.2) illustrates an example of a homogeneous but anisotropic and an isotropic but inhomogeneous patterns.

Evidence for isotropy comes from both large scale structure and the Cosmic Microwave Background (CMB). Fig. (1.3) demonestrates the isotropy of the CMB [1].

The assumption of spatial homogeneity combined with the observed isotropy leads uniquely to a FLRW (Friedmann-Lemaître-Robertson-Walker) metric. This metric is the exact solution of the Einstein equations for an expanding homogeneous & isotropic Universe. The FLRW metric has a zero Weyl tensor, and is, therefore, conformally flat. The metric can, therefore, be written as Minkowski times some function which gives the expansion of the Universe :

$$g_{\alpha\beta} = \begin{pmatrix} -a(\eta)^2 & 0 & 0 & 0 \\ 0 & a(\eta)^2 & 0 & 0 \\ 0 & 0 & a(\eta)^2 & 0 \\ 0 & 0 & 0 & a(\eta)^2 \end{pmatrix}, \tag{1.11}$$

[1]Although the CMB is isotropic to a good approximation, there are interesting differences and other apparent non-Gaussianities between the northern and southern hemispheres in the Wilkinson Microwave Anisotropy Probe (WMAP) [4, 5]. This makes the study of non-Gaussianity particularly interesting at this time.

University of Cape Town

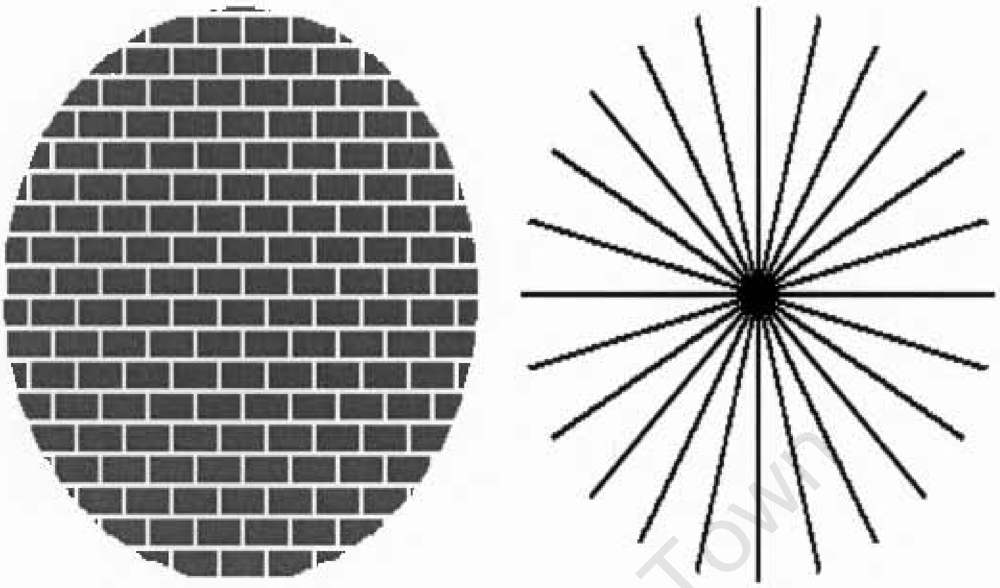

FIGURE 1.2: A homogeneous but anisotropic pattern on the left and an isotropic but inhomogeneous pattern on the right. If a space is isotropic about 3 or more points in 3 dimensions then it must also be homogeneous. Note that these figures display discrete translation and rotation symmetries while in cosmology we are interested in continuous symmetries, but the main ideas are the same. Image taken from *http://www.astro.ucla.edu/~ wright/cosmo_01.htm*

University of Cape Town

where we have introduced the conformal time $d\eta = dt/a(t)$. Using this metric in Einstein's equations Eq. (1.10), one can show that the Einstein equations reduce to just two equations; the Friedmann equation (H) and the acceleration equation ($\ddot{a}$) [2]

$$H^2 = \left(\frac{\dot{a}}{a}\right)^2 = \frac{8\pi G}{3}\rho - \frac{Kc^2}{a^2(t)} + \frac{\Lambda}{3} \tag{1.12}$$

$$\frac{\ddot{a}}{a} = -\frac{4\pi G}{3}(\rho + 3p)\,. \tag{1.13}$$

Where ρ is the density contributions from different components of matter; a is the scale factor, the expansion rate of the universe; p is pressure; K is the curvature constant of the Universe and Λ is the cosmological constant. We are using a unit system where $c = 1$. K takes three values depending on the curvature: 0 for flat curvature (eg. plane), -1 for negative curvature (eg. saddle) and $+1$ for positive curvature (eg. sphere). The different components of the universe are usually assumed to have a barotropic equation of state, $p = p(\rho)$. It is common to make

FIGURE 1.3: The CMB seen by COBE satellite. It has a uniform temperature of $T = 2.728$K (which is illustrated by the uniform red colour of the image) and is isotropic to one part in 10^5. This image is taken from *http://lambda.gsfc.nasa.gov*

University of Cape Town

an even stronger assumption of a linear relation, $p = w\rho$, where w can be time dependent in general. In this description normal matter has $w = 0$, radiation has $w = \frac{1}{3}$ and the cosmological constant has $w = -1$.

The critical density of the Universe at any redshift, z, is defined such that the density contributions from the matter components of the Universe at that z is enough to make space flat. This means we evaluate Eq. (1.12) with $K = 0$ and we get :

$$\rho_{\mathrm{crit}}(z) = \frac{3H(z)^2}{8\pi G}. \tag{1.14}$$

The density parameter of any component, x, in the Universe is then defined as

$$\Omega_x = \frac{\rho_x}{\rho_{\mathrm{crit}}}, \tag{1.15}$$

The conservation of energy implies an additional equation which is known as the continuity equation :

$$\dot{\rho} + 3H\rho(1 + 3w) = 0. \tag{1.16}$$

This can be integrated to give the evolution of the energy density :

$$\rho \propto \exp\left(-3\int_0^z \frac{1 + w(z')}{1 + z'}dz'\right), \tag{1.17}$$

where the redshift is related to the scale factor via $\frac{a}{a_0} = \frac{1}{1+z}$, where a_0 is the scale factor today.

In 1998 two groups [6, 7] independently have shown that the Universe is not only expanding but also accelerating. From Eq. (1.13) we see that acceleration of the Universe requires $(\rho + 3p) < 0$, and hence $w < -1/3$. Current data prefers an equation of state $w \simeq -1$ for a new component comprising approximately 70% of the Universe and is known as *Dark energy.*

1.2.1 The almost FLRW Metric

In a true FLRW Universe there are no galaxies or stars or any form of structure. The Universe we see, however, has all sorts of non-uniform structures, from solar systems to clusters of galaxies. Therefore to explain the observed Universe we require a metric that is not truly homogeneous. Fortunately, introducing small perturbations to the FLRW metric yields a good description of our Universe on large scales [8].

There are three types of perturbations that one can can make to the FLRW metric :

scalar which correspond to perturbations in the density, $\delta\rho$

vector perturbations corresponding to the T_{0i} terms which describe fluid vorticity

tensor corresponding to gravitational waves.

We only consider scalar perturbations since we are interested in large scale structure and hence will talk about Φ for the metric and $\delta\rho$ for the matter. In the longitudinal gauge the equation for the scalar perturbations in FLRW Universe is given by [9]

$$ds^2 = -(1 + 2\Phi)dt^2 + a(t)^2(1 - 2\Phi)dx_i dx^i \tag{1.18}$$

where $i = 1, 2, 3$ and Φ is the gravitational potential.

1.2.2 Distances in Cosmology

As we discussed in the first section of this chapter, the metric permits us to compute physical distances. Conversely if we measure distances we can learn

University of Cape Town

about the metric of spacetime. The two most important distances that we can measure in cosmology are the luminosity distance (d_L) and the angular diameter distance (d_A). We define the co-moving distance, $\chi(z)$, between the source and the observer via

$$\chi(z) = \int_0^z \frac{dz'}{H(z')}\,. \tag{1.19}$$

The angular diameter distance is inferred by measuring the angle that is subtended by an object whose physical length, l, is known. The angular diameter distance is very sensitive to the geometry of the metric and, hence, is a strong function of the curvature. The expression of this distance in a metric with curvature Ω_k today is given by [2]

$$d_A(z) = \frac{l}{\theta} = \begin{cases} \sinh\left[\sqrt{\Omega_k} H_0 \chi(z)\right] / \left[(1+z) H_0 \sqrt{|\Omega_k|}\right] & \Omega_k > 0 \\ \chi & \Omega_k = 0 \\ \sin\left[\sqrt{-\Omega_k} H_0 \chi(z)\right] / \left[(1+z) H_0 \sqrt{|\Omega_k|}\right] & \Omega_k < 0 \end{cases} \tag{1.20}$$

The luminosity distance is inferred by measuring the flux from an object of known luminosity. It is related to the angular diameter distance via

$$d_L(z) = (1+z)^2 d_A(z)\,. \tag{1.21}$$

Observationally the luminosity distance can be measured through standard candles such as Type Ia Supernovae [6] whereas the angular diameter distance can be measured through Baryon Acoustic Oscillations (BAO) [10] .

University of Cape Town

1.3 The Cosmic Microwave Background (CMB)

The detection of the CMB in 1965 by Penzias and Wilson [11] is one of the most important discoveries in the history of Cosmology. The CMB is the radiation that holds the footprints of the baby Universe. It has been stretched to the microwave region by the expansion of the Universe. It has an almost perfect black body spectrum with a precisely measured temperature of [3]

$$T_0 = 2.725 \pm 0.001 K\,. \tag{1.22}$$

A blackbody spectrum has an energy distribution function of the form

$$\rho_\gamma(\nu)d\nu = \frac{8\pi h\nu^3 d\nu}{e^{\frac{h\nu}{k_B T}} - 1} \tag{1.23}$$

where ρ_γ, k_B, h and ν are the energy density, Boltzmann constant, the Planck constant, and the photon frequency respectively.

The radiation density parameter Ω_γ is given by

$$\Omega_\gamma = \frac{\rho_\gamma}{\rho_{\text{crit}}} = 2.47 \times 10^{-5} h^{-2} \tag{1.24}$$

where ρ_{crit} is the critical density defined in Eq. (1.14). The temperature of the radiation in an expanding universe evolves as the inverse of the scale factor, $T \propto \frac{1}{a}$. Hence given the temperature of the CMB photons at some redshift, say today, we can calculate the temperature at another redshift, for example at $z = 10^3$ is

$$T = \frac{a_0}{a} T_0 = (1+z) T_0 \approx 3 \times 10^3 K \tag{1.25}$$

1.3.1 Matter-Radiation Equality

In addition to the dilution of the photon number density, the expansion of the Universe stretches the wavelength of the photons, and hence further reduces the energy. As a result $\rho_\gamma \propto a^{-4}$. The matter energy density on the other hand, decays only as $\rho_m \propto a^{-3}$. This faster decay of radiation relative to the matter yields an equivalence of the two energy densities at some early time, known as *matter-radiation equality*. The redshift of equality, z_{eq}, can be calculated by the following equation [12]

$$z_{eq} = 2.50 \times 10^4 (1 - \Omega_k) h^2 \left(\frac{T_{CMB}}{2.7}\right)^{-4} \tag{1.26}$$

where Ω_k is the curvature of the Universe.

University of Cape Town

1.3.2 CMB Recombination

The ionization energy of Hydrogen is given by

$$B_H = (m_e + m_p - m_H)c^2 = 13.6eV \quad . \tag{1.27}$$

Where m_e, m_p, m_H are the electron, proton and Hydrogen masses respectively. When the temperature of the Universe was larger than this energy, the photons ionized essentially all hydrogen atoms via the reaction :

$$H + \gamma \rightarrow p + e^- \tag{1.28}$$

Photons scatter efficiently off the free electrons through Thomson scattering which forced the photons to perform a random walk with a short mean free path of $\approx 1/n_e\sigma_T$, where n_e is the number density of free electrons and $\sigma_T = 0.665 \times 10^{-2} cm^2$ is the Thomson scattering cross section.

As the Universe expanded and cooled the reaction, Eq. (1.28), became inefficient and the protons combined with free electrons to form neutral hydrogen in a process known as recombination. Without free electrons to scatter from, the photons decoupled: the mean free path of the photons became very large. This occurred at $z \approx 1089$ over a period of $\Delta z \approx 80$. In the approximation where we consider decoupling to be instantaneous ($\Delta z \rightarrow 0$), we talk about decoupling occurring on the *the surface of last scattering.*

University of Cape Town

1.3.3 Temperature Anisotropies of the CMB

After the discovery of the cosmic microwave background, Sachs & Wolfe (1967) [13] predicted that the CMB temperature has temperature anisotropies of order $\frac{\Delta T}{T} \sim 10^{-2}$, which is larger than the observed anisotropy by a factor of $\sim 10^3$.

Silk (1967) [14] calculated the density perturbations needed at the surface of last scattering, to produce galaxies. By converting this perturbation to the gravitational potential via Poisson's equation, he predicted $\frac{\Delta T}{T} \sim 3 \times 10^{-4}$ on arcminute scales. He also showed that the imperfect coupling between photons and baryons on small scales leads to a damping of anisotropies on small angular scales. This phenomenon is called *Silk damping.* His prediction was still an order of magnitude larger than the true value.

All treatments of the CMB anisotropies before 1982 were done only in the context of photons and baryons. However, the inclusion of dark matter by Uson & Wilkinson in 1982, pushed the anisotropy predictions down to $\frac{\Delta T}{T} \sim 4 \times 10^{-5}$, on 1.5 arcminutes scale.

The COsmic Background Explorer (COBE) satellite mission [15] in 1992 experimentally confirmed for the first time that the CMB anisotropies on large angular scales are $\sim 10^{-5}$. Subsequent high-precision balloon and satellite CMB experiments such as BOOMERanG and WMAP measured the anisotropies with unprecedented accuracy. The angular power spectrum from recent CMB experiments is shown in Fig. (1.4)

University of Cape Town

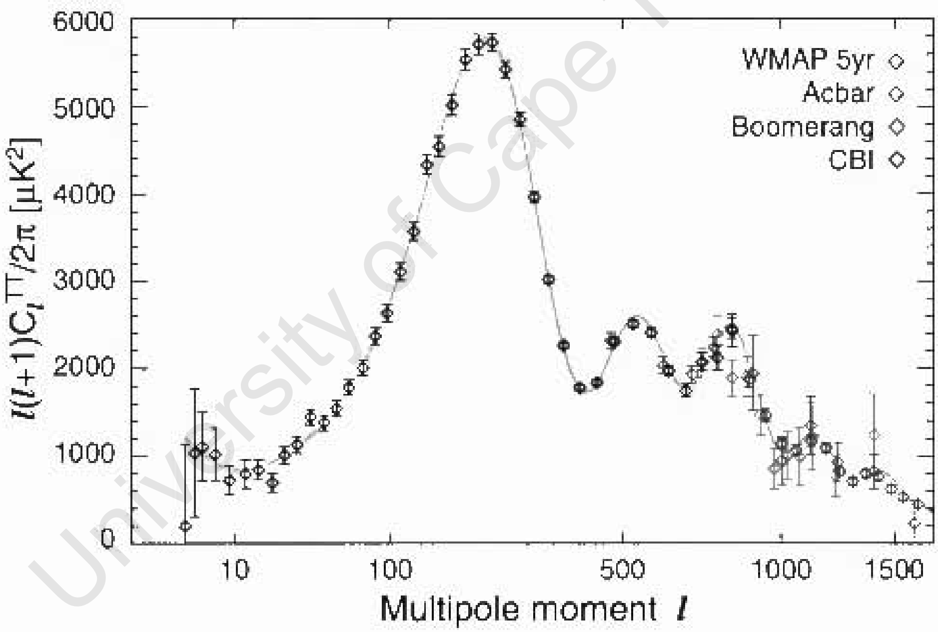

FIGURE 1.4: The CMB temperature (TT) angular power spectrum from the WMAP 5-year, Acbar, Boomerang and CBI experiments. The red curve is the best-fit theory spectrum with cosmic parameters $(\Omega_b h^2, \Omega_m h^2, \Delta_R^2, n_s, \tau, H_0) = (0.0227, 0.131, 2.41, 0.961, 0.089, 72.4)$. [16]

To understand the angular power spectrum of the CMB we first expand the temperature anisotropies in spherical harmonics as

$$\frac{\Delta T}{T}(\theta, \phi) = \sum_{l=1}^{\infty} \sum_{m=-l}^{l} a_{lm} Y_{lm}(\theta, \phi), \tag{1.29}$$

where θ and ϕ are the spherical co-ordinates, which represent a point on a sphere. The coefficients of this expansion, a_{lm}, are a measure of the irregularities at different angular scales with the multipole l roughly corresponding to an angle of $\frac{180^o}{l}$ in the sky. By using the inversion formula, we can write the coefficients as

$$a_{lm} = \int_{-\pi}^{\pi} \int_{0}^{\pi} \frac{\Delta T}{T}(\theta, \phi) Y^{*}_{lm}(\theta\, \phi) \sin(\theta) d\theta d\phi \,. \tag{1.30}$$

The angular power spectrum of the CMB is defined to be the second moment of the a_{lm}.

$$C_l = \langle \mid a_{lm} \mid^2 \rangle \tag{1.31}$$

Fig. (1.5) shows plots of the CMB from the WMAP 3-year data.

1.3.4 Primordial Non-Gaussianity in the CMB

Non-linear perturbations in the initial density perturbations or non-linear structure growth after decoupling can lead to a non-Gaussian CMB anisotropy today. Therefore the study of non-Gaussianity in the CMB can put some constraints on these two effects. The problem then is if we detect non-Gaussianity, can we break the degeneracy between the two effects? The answer is yes. This is because the non-Gaussianity from primordial non-linear perturbations and the non-Gaussianity from secondary effects have their own unique signatures that can easily be disentangled. In this section we will briefly discusses primordial non-Gaussianity in the context of the CMB.

The standard cosmological model for the generation of primordial density perturbations is inflation. In this model the mechanism that generates density fluctuations is a period of exponential expansion following the Big Bang. The seeds of the perturbations are produced by the quantum fluctuations when the universe was 10^{-34} seconds old. The standard main assumption is that the fluctuations are scale independent and has a Gaussian distribution. This assumption is very well justified by the current CMB and large scale structure data despite the fact that small levels of non-Gaussianity are not ruled out. The search for primordial non-Gaussianity is extremely difficult as it requires very high resolution experiments with techniques to correctly estimate the amount.

University of Cape Town

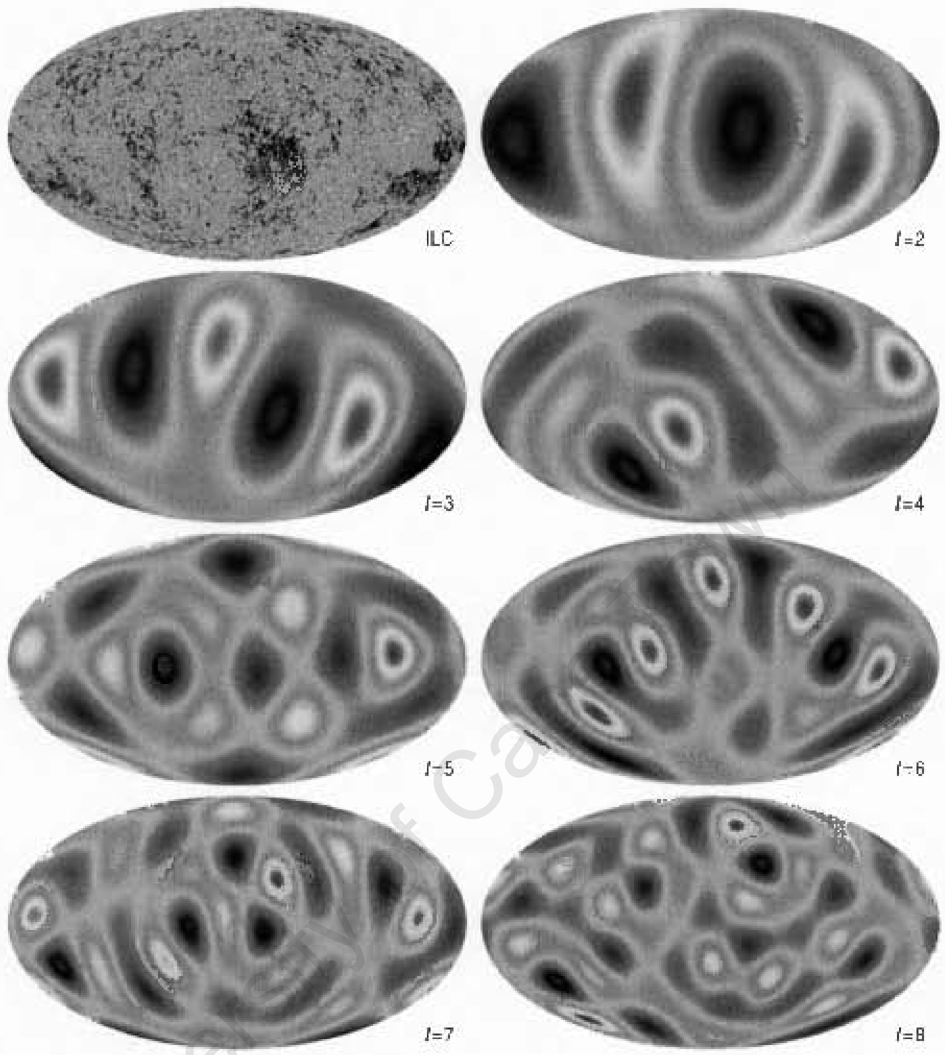

FIGURE 1.5: The 3-year WMAP maps of power spectrum modes for the first few multipols, $l = 2-8$. The top left figure is the temperature map of the microwave background computed from full-sky fits. The other figures encode structure on a particular scale, add up to the large-scale structure of the CMB sky. Careful observation of this figures suggests that hot and cold spots are not distributed randomly, implying a preferred direction in the cosmos, the '*axis of evil*'. If confirmed, this is inconsistent with Gaussian random-phase fluctuations, which is predicted by standard inflationary model. This picture is taken from [17].

The popular form of primordial non-Gaussianity that many people use assumes that the primordial curvature potential is given by

$$\Phi(x) = \Phi_L(x) + f_{NL}[\Phi_L^2(x) - \langle\Phi_L^2(x)\rangle] \tag{1.32}$$

Where $\Phi_L(\mathbf{x})$ is the Gaussian part of the primordial curvature perturbation. The coupling constant f_{NL} quantifies the amount of primordial non-Gaussianity. The Gaussian case is recovered when $f_{NL} = 0$. The aim of the study of primordial non-Gaussianity is therefore to put a stringent constraint on this parameter. The current best constraint on f_{NL} comes from the WMAP data. The 5-year result yields $-9 < f_{NL} < 111$ with 95% Confidence Limit (CL) [18] while Yadav & Wandelt (2008) [19] find a positive detection of f_{NL} with 95% CL from the 3-year WMAP data, $27 < f_{NL} < 147$. Also recently Smith *et al.* [20] find $-4 < f_{NL} < 80$ with 95% CL using the optimal estimator for f_{NL}^{local} to the 5-year WMAP data. Constraints on non-Gaussianity from large scale structure are not as strong as the CMB. However, searches for scale-dependent bias induced by non-Gaussianity yield constraints of $-29 < f_{NL} < 70$ (95% CL) [21] with weaker constraints still reported in other studies [22].

Since the power spectrum of a given field doesn't contain any phase information, the second moment of a_{lm} cannot tell us about non-Gaussian information. To study non-Gaussianity, therefore, we need to consider the higher order moments. The lowest order moment that encapsulates the non-Gaussian information is the third moment of a_{lm}, called the *bispectrum*. Moreover, this function satisfies a null hypothesis: it is zero for Gaussian fields. Therefore the bispectrum [23, 24, 25, 26] is an excellent choice for studying non-Gaussianity. Other statistics that people use to study primordial non-Gaussianity include the *trispectrum* [27, 28, 29], *Minkowski Functionals* [30, 31], *Wavelets.* [32]

1.4 Inflation

What seeds the initial perturbations of the Universe? Why is the Universe isotropic on large scales? Why is the curvature of the Universe very close to flat? These are known as the structure, horizon and flatness problems respectively. The theory of inflation was invented in 1981 to try to solve these problems [33, 34, 35].

University of Cape Town

1.4.1 Conditions for inflation

Inflation requires that the Universe underwent a sustained period of acceleration before Big Bang Nucleosynthesis. From Eq. (1.13) we have

$$\frac{\ddot{a}}{a} = -\frac{4\pi G}{3}(\rho + 3p) \tag{1.33}$$

Therefore for $\ddot{a} > 0$, the pressure has to be negative with the equation of state satisfying, $w < -1/3$. A scalar field can naturally satisfy these conditions.

The dynamics of a scalar field (with a canonical kinetic term) is described by the Klein-Gordon equation, which in a FLRW metric is given by:

$$\ddot{\phi} + 3H\dot{\phi} + \frac{\partial V}{\partial \phi} = 0 \tag{1.34}$$

where H is the Hubble parameter and $V(\phi)$ is the potential for the field which primarily controls the dynamics of the field. The energy density and pressure are given by

$$\begin{aligned} \rho &= \tfrac{1}{2}\dot{\phi}^2 + V(\phi) \\ p &= \tfrac{1}{2}\dot{\phi}^2 - V(\phi) \end{aligned} \tag{1.35}$$

The equation of state of the scalar field can then be written as

$$w = \frac{p}{\rho} = \frac{\frac{1}{2}\dot{\phi}^2 - V(\phi)}{\frac{1}{2}\dot{\phi}^2 + V(\phi)} \tag{1.36}$$

When we impose the condition $\frac{1}{2}\dot{\phi}^2 \ll V(\rho)$, known as the slow-roll approximation, we get a negative equation of state for the scalar field and hence acceleration. Physically this approximation means the potential of the field is sufficiently flat that the scalar field varies only slowly. For successful inflation we must also demand that the scalar field continues rolling very slowly. To ensure that we exit inflation, the first derivative of the potential must not vanish. Moreover, the second derivative of the potential should be negligible when compared to the first derivative. As a result the kinetic energy term will have a finite but small value and $w > -1$.

University of Cape Town

The Friedmann equation and its derivative for the scalar field from Eq. (1.35) and Eq. (1.12) in flat FLRW space read as

$$\begin{aligned} H^2 &= \frac{8\pi G}{3}\left(\frac{1}{2}\dot{\phi}^2 + V(\phi)\right) \\ \dot{H} &= -4\pi G\dot{\phi}^2 \end{aligned} \tag{1.37}$$

The concept of slow-roll can be well described mathematically by defining the so-called slow-roll parameters [9]

$$\epsilon = \frac{1}{16\pi G}\left(\frac{V_\phi}{V}\right)^2 \tag{1.38}$$

$$\eta = \frac{V_{\phi\phi}}{8\pi G V} \tag{1.39}$$

$$\xi^2 = \frac{V_\phi V_{\phi\phi\phi}}{64\pi^2 G^2 V^2} \tag{1.40}$$

where $V_\phi \equiv \mathrm{d}V/\mathrm{d}\phi$, etc..

For the slow-roll approximation to hold these parameters must be much smaller than one.

The scale factor for inflation takes a quasi-exponential form of

$$a(t) = a_0 e^{\int H dt} \tag{1.41}$$

a_0 in this equation is the scale factor at the beginning of inflation and H is the Hubble parameter. In the limit $H \to const.$, $a(t) \to a_0 e^{Ht}$. The duration of inflation is commonly measured by the number of e-folds, N, given by

$$N = \int H dt. \tag{1.42}$$

The larger the number of the e-folds, the longer the inflationary phase. Beside the condition that $\ddot{a} > 0$, we need inflation to last for at least 60 e-folds to solve the horizon and flatness problems [9] . Fig. (1.6) illustrates how inflation solves the horizon problem. In the inflationary scenarios quantum fluctuations during inflation provide the seed for large scale structure. The amplitude of these fluctuations is approximately [36, 37]

$$\delta\Phi_k = \frac{H}{2\pi}|_{k=aH} \tag{1.43}$$

University of Cape Town

Since the Hubble rate changes very slowly during inflation we see that inflation predicts a nearly scale invariant spectrum of perturbations. These fluctuations are also typically Gaussian. Any deviations from these two predictions provide a good way of discriminating between different inflationary models.

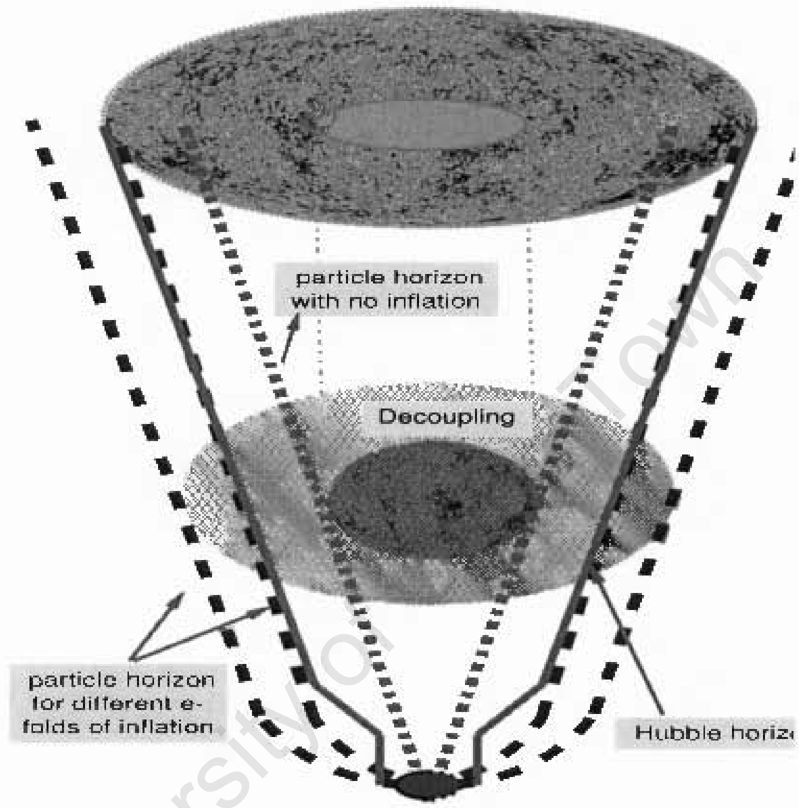

FIGURE 1.6: This figure shows the horizon problem and its solution from inflation by schematically illustrating the scales that would be in casual contact at decoupling with and without inflation. The key idea of the horizon problem is that a Universe with only matter and radiation epochs, the Hubble scale is larger than the particle horizon. The particle horizon is defined by the distance that light can travel since the Big-Bang. Hence scales larger than the particle horizon but inside the Hubble scale were not in casual contact since the big-bang. This results in an anisotropy in the large scale, contrary to the isotropy seen in the CMB. Inflation solves this problem by assuming a rapid inflationary phase at the early Universe such that the quantum fluctuations before inflation were pushed out the Hubble scale and re-enter again at a later stage.

University of Cape Town

1.4.2 Primordial non-Gaussianity from inflation

Models of inflation are broadly classified into two groups based on the physical mechanisms they use to generate primordial non-Gaussianity. Models that generate non-Gaussianity at horizon crossing by non-linear perturbations in the inflaton field are called **non-local**. Models that generate non-Gaussianity by mode-mode couplings of an extra field with the inflaton field, outside the horizon, are called **local** [26, 38, 39, 40, 41]. We discuss specific examples of each case below. The usual form assumed for the curvature perturbation with small deviations from Gaussianity is a quadratic function of the dominant linear Gaussian fluctuation, Φ_L:

$$\Phi(x_\mu) = \Phi_L(x_\mu) + f_{\rm NL}[\Phi_L^2(x_\mu) - \langle\Phi_L^2(x_\mu)\rangle] \ , \tag{1.44}$$

where the weak coupling parameter, $f_{\rm NL}$, quantifies the amount of non-Gaussianity from inflation, ($f_{\rm NL} = 0$ corresponds to the Gaussian case.)

For a field with small departures from Gaussianity, the bispectrum, which is the 3-point correlation function in Fourier space, is the most sensitive of the higher order statistics [41]. The local and non-local types of non-Gaussianities introduced above have the peak of their corresponding bispectra for different triangular configurations. For the local type the peak is for the so-called squeezed configurations, where the triangle, in Fourier space, consists of two long sides and one short side ($k_1 \ll k_2, k_3$). Non-local non-Gaussianity in contrast, peaks for equilateral triangular configurations ($k_1 \sim k_2 \sim k_3$) [26, 38, 39, 40, 41]. We now briefly discuss non-Gaussian predictions for various models of inflation.

University of Cape Town

1.4.2.1 Single field models

The simplest models of inflation rely on a single scalar field with action [42] :

$$S = \int d^4x[-\frac{1}{2}F(X) - V(\phi)] \ . \tag{1.45}$$

where, as before, $V(\phi)$ is the potential, $X \equiv \nabla_\mu\phi\nabla^\mu\phi$ and $F(X)$ is an arbitrary kinetic function. Standard chaotic and new inflation models use a canonical kinetic term ($F(X) = X$). During slow-roll, the non-Gaussianity induced in these models is very small, estimated to be [25, 39]:

$$f_{NL} = 3\epsilon - 2\eta \quad . \tag{1.46}$$

As a result the simplest models of inflation predict tiny levels of non-Gaussianity ($f_{NL} \sim 10^{-2}$) that are amplified to $O(1)$ by the post-inflationary evolution [43]. Nevertheless, such small values will remain undetectable for the next decade or so.

If, however, one considers models with non-canonical kinetic terms $F(X) \neq X$, then the nonlinearity of the kinetic term induces a much larger level of non-Gaussianity which will be measureable in the next decade [39, 41].

1.4.2.2 Multiple field models of inflation

Another class of models which leads to interesting levels of non-Gaussianity is that with many light fields (here light refers to the mass of the field relative to the Hubble scale) [44, 45]. In that case the key difference compared with the single field case is the possibility of large scale entropy or isocurvature fluctuations whose statistics need not be of Gaussian form even if the adiabatic perturbation is Gaussian [39, 45].

An example is the curvaton model where a second field is light during inflation and acquires a scale-invariant spectrum of entropy perturbations. After inflation this field becomes dynamically important and the entropy perturbations are converted to adiabatic fluctuations but with significant non-Gaussianity. In these models the non-Gaussianity is of local type.

University of Cape Town

Chapter 2

Statistics and Evolution of Gravitational Clustering

In this second introductory chapter we present a literature review of the first and the second order cosmological perturbations together with the statistical methods used to quantify it from observation.

2.1 Introduction

The evolution of an exact FLRW universe is the same as the Newtonian equation of an isolated sphere with mean density, $\bar{\rho}$, equal to that of the FLRW universe [46].

In the absence of any perturbations in the density, the evolution equations of the Universe reduce to only three linear equations that describe the density, expansion and velocity:

$$\rho = \frac{\rho_0}{a^3} \tag{2.1}$$

$$r = a\chi \tag{2.2}$$

$$u = \frac{\dot{a}}{a} r = Hr\,, \tag{2.3}$$

where χ is the co-moving distance, u is the velocity and H is the Hubble parameter. Eq.(2.3) is known as the Hubble law. Unfortunately, there are no such simple solutions for a perturbed cosmos.

University of Cape Town

The general evolution equations of the perturbations for an ideal fluid are governed by three partial differential equations known as the *continuity*, *Euler*, and *Poisson* equations. In a co-moving coordinate system these equations are given by [46]

$$\begin{aligned}
&\frac{\partial \delta}{\partial t} + \frac{1}{a}\nabla . \left[(1+\delta)\mathrm{v}\right] = 0 \\
&\frac{\partial \mathrm{v}}{\partial t} + \frac{\dot{a}}{a}\mathrm{v} + \frac{1}{a}(\mathrm{v}\cdot\nabla)\mathrm{v} = -\frac{1}{a}\nabla\Phi \\
&\nabla^2\hat{\Phi} = 4\pi G\bar{\rho}a^2\delta
\end{aligned} \tag{2.4}$$

where $\delta = \frac{\rho-\bar{\rho}}{\bar{\rho}}$ is the fractional density, $\mathbf{v}$ is the Hubble flow velocity, and Φ is the gravitational potential. Fourier transforming these equations gives

$$\begin{aligned}
&\frac{\partial \delta}{\partial t} + \frac{1}{a}\left(ik\cdot v_k + \sum_{k'} i\delta_{k'}\cdot v_{k-k'}\right) = 0 \\
&\frac{dv_k}{dt} + \frac{\dot{a}}{a}v_k + \frac{1}{a}\sum_{k'} i\left[v_{k'}\cdot(k-k')v_{(k-k')}\right] - i\frac{k}{a}\Phi = 0 \\
&k^2\Phi_k = -4\pi a^2\bar{\rho}\delta_k
\end{aligned} \tag{2.5}$$

The summations in these equations are the result of couplings between the different Fourier modes, which reflect the non-linearity of the gravitational instability.

2.2 Linear Perturbation Theory (LPT)

The Taylor expansion of δ is given by

$$\delta = \delta^{(1)} + \delta^{(2)} + .. \tag{2.6}$$

where $\delta^{(n)} = O((\delta^{(1)})^n)$. In linear perturbation theory the density contrast δ is assumed to be very small, $\delta \ll 1$, hence we consider only the first order term in the expansion.

Since we know that fluctuations at small scales today are large, the linear perturbation theory is valid only at large scales or at early times where the perturbation was not amplified by gravitational collapse. The coupling terms in Eq. (2.5) on large scales are very small and can be neglected. The Euler and continuity

University of Cape Town

equations Eq. (2.5) in the case of dust can be combined to yield

$$\frac{\partial^2 \delta_k}{\partial t^2} + 2\frac{\dot{a}}{a}\frac{\partial \delta_k}{\partial t} = 4\pi G\bar{\rho}\delta_k\,. \tag{2.7}$$

The solution of this equation during matter domination can be found by assuming a polynomial expansion for δ and writing $4\pi G\bar{\rho} = \frac{3}{2}H^2\Omega_m$, where $\Omega_m = \frac{\bar{\rho}}{\rho_{crt}}$. The time evolution of the linear density can then be written as

$$\delta_k = D_1 t^{\frac{2}{3}} + D_2 t^{-1}. \tag{2.8}$$

This implies that the density field has both a growing and a decaying mode. However, since the second term decays rapidly as the universe expands, it can be safely neglected at late times. Eq. (2.8) can then be written as

$$\delta^{(1)} = D(t)\delta^{(0)}(x) + \textbf{decaying mode} \tag{2.9}$$

Where $\delta^{(0)}(x)$ is the initial density contrast and $D(t)$ is the growth function. The growth function in flat FLRW Universe satisfies [17]:

$$D(z) = \frac{5\Omega_m E(z)}{2}\int_z^\infty \frac{(1+z')}{E(z')^3}dz'\,. \tag{2.10}$$

Where

$$E(z) = H/H_0 = \sqrt{\Omega_m(1+z)^3 + \Omega_{DE}f(z) + \Omega_k(1+z)^2} \tag{2.11}$$

and Ω_m, Ω_{DE}, Ω_k are the present values of the fractional matter, dark energy and curvature density, respectively. The dark energy density evolution parameter, $f(z)$, is given by:

$$f(z) = \exp\left[-3\int_0^z \left(\frac{1+w(z)}{1+z}\right)\right] \tag{2.12}$$

In pressure-free linear perturbation theory, the growth of different modes is independent of scale in that all modes grow by the same amount through time.

2.3 Second Order Perturbation Equations (2OPT)

In second order perturbation theory we consider the Taylor expansion of the density field up to the second order, $\delta = \delta^{(1)} + \delta^{(2)}$. In this theory, the mode-mode

University of Cape Town

couplings in Eq.(2.5) will not vanish, which significantly complicates the evolution of the perturbations. In general the density perturbations with the second-order corrections are given by [40, 48]

$$\delta_{\mathbf{k}} = \delta^L_{\mathbf{k}} + \int d^3q F_2(\mathbf{q}, \mathbf{k}-\mathbf{q}) \delta^L_{\mathbf{q}} \delta^L_{\mathbf{k}-\mathbf{q}} \tag{2.13}$$

where $\delta^L_{\mathbf{k}}$ is the linear order and the kernel $F(\mathbf{k_1}, \mathbf{k_2})$ is given in an Einstein-deSitter by:

$$F(\mathbf{k_1}, \mathbf{k_2}) = \frac{5}{7} + (\frac{k_1}{k_2} + \frac{k_2}{k_1})\frac{x}{2} + \frac{2}{7}x^2 \,. \tag{2.14}$$

Here x is the cosine of the angle between k_1 and k_2 vectors.

2.4 Fourier Space Correlation Functions

To describe the statistical properties of an arbitrary density field, we can use the hierarchy of Fourier space correlation functions given by

$$\begin{aligned} P(k_1, k_2) &= \langle \delta_{k_1} \delta_{k_2} \rangle \\ B(k_1, k_2, k_3) &= \langle \delta_{k_1} \delta_{k_2} \delta_{k_3} \rangle \qquad (2.15) \\ T(k_1, k_2, k_3, , k_4) &= \langle \delta_{k_1} \delta_{k_2} \delta_{k_3} \delta_{k_4} \rangle \qquad (2.16) \\ &\ldots \end{aligned}$$

which are known as the power spectrum, bispectrum, trispectrum etc. The angles $\langle \ldots \rangle$ represent a statistical ensemble average. Unfortunately we can not compute ensemble averages in Cosmology as there is only one Universe, and we must assume ergodicity to replace ensemble averages with spatial volume averages [49].

For a Gaussian density field all the odd order correlation functions vanish and all the even order correlation functions can be written in terms of the power spectrum.

The density (δ) and the potential (Φ) fields are related by Poisson's equation

$$\delta(k, z) = -\frac{3k^2}{5H_0^2\Omega_m} T(k) D_+(z) \Phi^{prim}_k \,. \tag{2.17}$$

University of Cape Town

Where $T(k)$ is the transfer function and $D_+(z) = (1+z)D(z)$. The linear density power spectrum at redshift z is then related to the primordial power spectrum via:

$$P_L(k) = T^2 D_+^2(z) P_\delta^{prim}(k) \tag{2.18}$$

$$= \frac{9k^4}{25 H_0^4 \Omega_m^2} T^2(k) D_+^2(z) P_\Phi^{prim}(k)) \,. \tag{2.19}$$

Here $P_\delta^{prim}(k) = A|\delta_k^{(0)}|^2$ and $P_\Phi^{prim}(k) = A'|\Phi_k^{prim}|^2$ are the primordial density and potential power spectra, respectively.

Because observationally we typically trace the dark matter through luminous galaxies, the galaxy power spectrum we measure is a biased tracer of the dark matter power spectrum. This means the galaxy and the underlying matter power spectrum are not the same but are related by some type of bias function. In the local bias model [50, 51, 52] we assume that the galaxy denisty field is a Taylor expansion of the underlying dark matter density field.

$$\delta_g = b_1 \delta_m + b_2 \delta_m^2 + \dots \tag{2.20}$$

The term that survives in the linear theory is the the first order bias term, b_1, which commonly is just written as simply b. In this approximation, this relation between the galaxy and matter power spectra can be written as :

$$P_{gal}(k,z) = b^2 P_m(k,z) \,. \tag{2.21}$$

2.4.1 Phase Correlations and the Bispectrum

Mode-mode coupling in 2OPT generates information that can not be characterised by the power spectrum alone. The resulting non-Gaussianities induce non-zero odd-order correlation functions. The bispectrum (the three point correlation function in Fourier space) in 2OPT is given by [40, 48]:

$$B(k_1,k_2,k_3) = 2F(k_1,k_2)P_L(k_1)P_L(k_2) + cyc. \tag{2.22}$$

Where $P_L(k)$ is the linear power spectrum given by Eq.(2.18).

If we write $\delta_k = a_k e^{i\theta k}$, the power spectrum is just $P(k) \propto |a_k|^2$, which clearly carries no information about the phases θ_k. In the Gaussian case, the θ_k are drawn

University of Cape Town

FIGURE 2.1: Effect of the phase information. The first column in this figure shows two original pictures of human faces. In the second column the faces are reconstructed by throwing away the phase information from the original picture, assuming all the information is characterized by the power spectrum. In the third column the faces are reconstructed from the amplitude of the original face and the phase of the other face. These pictures are taken from [53].

from a uniform random distrubtion and indeed carry no information. However this is no longer true in the non-Gaussian case. Phases of a non-Gaussian field carry all of the non-Gaussian information. Fig.(2.1) shows the relative information content stored in the phase and amplitude of a human face. From this figure we can see that most of the information that enables us to identify a particular face comes from the phase information rather than the amplitude. The first column in this figure shows pictures of two human faces. In the second column the faces are reconstructed by using the power spectra from the original pictures, but with phases generated from a uniform random distrubtion (ie. the Gaussian approximation). In the third column the faces are reconstructed, this time swaping the phases of the original faces while keeping their original amplitude unchanged. Clearly phase information dominates, showing how drastic the Gaussian approximation can be.

Similarly Fig.(2.2) shows an N-body simulation of large scale structure with and

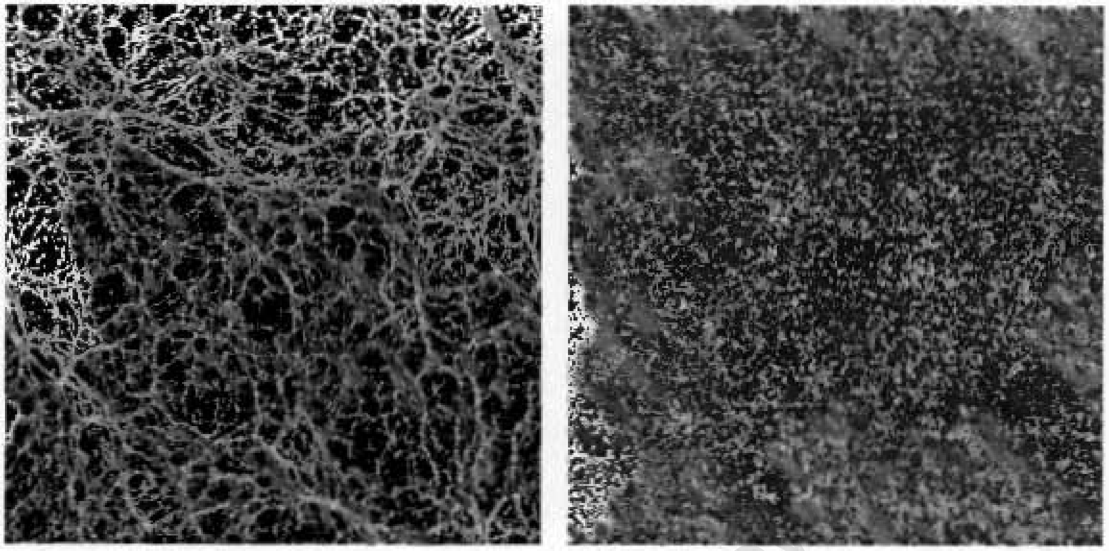

FIGURE 2.2: Numerical simulation of galaxy clustering (left) together with a version generated by randomly reshuffling the phases between Fourier modes of the original picture (right). These pictures are taken from [49].

without a reshuffling of the phase information of the simulation. We can see from these plots that a large amount of the clustering information of the simulation is stored in the phase of the modes. Once we randomly reshuffle the phases of the modes in the density field, the information of clustering is significantly degraded.

2.5 Statistics on the Sphere

The angular power spectrum is the Legendre transform of the two point angular correlation function. Any square integrable function on the unit sphere can be expressed by the linear combination of the spherical harmonics, Y_{lm}. A function is said to be square integrable if the integral of the square of its absolute value exists and is finite. The definition of declination (Dec), θ, and right ascension (RA), ϕ, we use in this thesis are $0 < \theta < \pi$ and $0 < \phi < 2\pi$. We can expand an arbitrary field in terms of spherical harmonics as

$$\sigma(\theta, \phi) = \sum_{l,m} a_{lm} Y_{lm}(\theta, \phi) \tag{2.23}$$

University of Cape Town

where the Y_{lm}'s are the spherical harmonics, which are the eigenfunctions of the Laplace equation on the sphere. Mathematically they are given by:

$$Y_{lm} = N_{lm} P_{lm}(cos(\theta)) \exp{(im\phi)}\,. \tag{2.24}$$

where $N_{lm} = \sqrt{(\frac{(2l+1)(l+1)}{4\pi(l-1)})}$ is the normalization factor and P_{lm} are the associated Legendre polynomials. Using the orthonormal nature of Y_{lm}, we can write the a_{lm} coefficients as:

$$a_{lm} = \int_{\Delta\Omega} \sigma(\theta,\phi) Y_{lm}(\theta,\phi) d\Omega \tag{2.25}$$

where $d\Omega = \sin(\theta)d\theta d\phi$ is the solid angle and the integrations is over the observed sky, $\Delta\Omega$. To compute this parameter we use the same estimator as that of [54]

$$A_{lm} = \sum_{\theta,\phi} Y^{*}_{lm}(\theta,\phi)\,. \tag{2.26}$$

where θ and ϕ in this case are coordinate points of the observed sky.

The angular power spectrum, C_{lm}, and bispectrum, $B^{m_1 m_2 m_3}_{l_1 l_2 l_3}$, of a density field on a sphere are given by ensemble average of the second and third moment of the spherical harmonic coefficients a_{lm}, respectively:

$$\begin{aligned} C_{lm} &= \langle a_{lm} a^{*}_{lm} \rangle \\ B^{m_1 m_2 m_3}_{l_1 l_2 l_3} &= \langle a_{l_1 m_1} a_{l_2 m_2} a_{l_3 m_3} \rangle \end{aligned} \tag{2.27}$$

where * is a complex conjugate

For statistically homogeneous and isotropic field the spherical harmonic coefficients, a_{lm}'s, are drawn from a Gaussian distribution [55, 56]. This means the non-diagonal terms of $\langle a_{l_1 m_1} a_{l_2 m_2} \rangle$ are zero. Also $\langle a_{lm} \rangle = 0$ for $l \neq 0$. The angular power spectrum averaged over m can then be written as.

$$\begin{aligned} C_l &= \frac{1}{(2l+1)} \sum_m C_{lm} \\ &= \frac{1}{(2l+1)} \sum_m \langle |a_{lm}|^2 \rangle \end{aligned} \tag{2.28}$$

If the function $\sigma(\theta,\phi)$ is statistically isotropic, the information from $-l \leq m < 0$ are redundant. Averaging over $0 < m < l$ or $-l < m < l$ doesn't make any difference as each value of m should give an independent estimate of a_{lm}. Averaging over $-l < m < l$ just reduces the overall error. In fact, the result for $-m$ should be identical to the result for $+m$, because the original density field is real. So $0 < m < l$ is in fact the full set of independent measurements we can get from C_l.

The bispectrum given in Eq.(2.27) is defined by triangles on a sphere with sides l_1, l_2, l_3. The number of possible triangles on a sphere is infinite. Fortunately, because of the various symmetries and correlations due to isotropy, the total number of independent triangles reduces to some finite number. The subsets of triangles that are independent can be imposed by writing the angular average bispectrum as follows [23, 24]:

$$B_{l_1 l_2 l_3} = \sum_{m_1, m_2, m_3} \begin{pmatrix} l_1 & l_2 & l_3 \\ m_1 & m_2 & m_3 \end{pmatrix} a_{l_1 m_1} a_{l_2 m_2} a_{l_3 m_3} \tag{2.29}$$

Where the matrix between big brackets is the Wigner-3j symbol which ensures that the following conditions are satisfied:

1. $|l_i - l_j| \leq l_k \leq l_i + l_j$
2. $l_1 + l_2 + l_3 = even$
3. $m_1 + m_2 + m_3 = 0$

We now discuss shot noise and error estimates on measurements of the power spectrum and bispectrum.

2.5.1 Shot Noise

The shot noise, which corresponds to the $l = 0$ in Eq.(2.25), is the surface density of objects per steradian and is a special case. The only harmonic in it is $m = 0$, and $Y_{00} = \frac{1}{\sqrt{4\pi}}$. It can be written as $\sigma_0 = \langle a_{00} \rangle = \frac{N}{\Delta\Omega}$, where N is the total number of points from which the density field is constructed and $\Delta\Omega$ is the area of the sky observed. The contribution of the shot noise to the angular power spectrum is therefore given by

$$shot\ noise(C_l) = \sigma_0\,. \tag{2.30}$$

University of Cape Town

Similarly we calculated the contribution of the shot noise to the bispectrum and it is given by

$$shot\ noise(B_{l_1 l_2 l_3}) = \sqrt{\frac{(2l_1+1)(2l_2+1)(2l_3+1)}{4\pi}} \begin{pmatrix} l_1 & l_2 & l_3 \\ 0 & 0 & 0 \end{pmatrix} \sigma_0 \, . \tag{2.31}$$

Hence, the final C_l and $B_{l_1 l_2 l_3}$ can be found by subtracting these shot noise contributions from Eq.(2.28) and Eq.(2.29), respectively. Note that since we are working using the overdensity field parameter, $\sigma = \frac{\rho - \bar{\rho}}{\bar{\rho}}$, we divide the final equations for the power spectrum and bispectrum by $1/\sigma_0^2$ and $1/\sigma_0^3$, respectively.

2.5.2 Error Bars

The errors on the angular power spectrum and bispectrum can be approximated as [57].

$$\sigma(C_l) = \frac{1}{\sqrt{(l+0.5)}} \frac{1}{(C_l + \frac{1}{\sigma_0})} \tag{2.32}$$

$$\sigma(B_{l_1 l_2 l_3}) = \sqrt{\left(C_{l_1} + \frac{1}{\sigma_0}\right)\left(C_{l_2} + \frac{1}{\sigma_0}\right)\left(C_{l_3} + \frac{1}{\sigma_0}\right)\Delta_{l_1,l_2,l_3}} \tag{2.33}$$

where $\Delta_{l_1,l_2,l_3} = (1+\delta_{l_1 l_2})(1+\delta_{l_1 l_3})(1+\delta_{l_2 l_3})$ and it is 6, 2, 1 when three, two and none of the sides are equal, respectively. δ_{ij} is the Kronecker-delta function. In the presence of a sky cut, Eq. (2.32) &, (2.33) will be modified by $1/f_{sky}$ factor to account the incompletness [24]. Where

$$f_{sky} = \frac{\text{area of the observed sky}}{4\pi}$$

is the ratio of the area of the observed sky to the full sky.

University of Cape Town

Chapter 3

The MegaZ-LRG Catalogue

University of Cape Town

In this chapter we present both a literature review and a power spectrum analysis of the MegaZ-LRG Catalogue [54, 58]. Our power spectrum code reproduces some of the results found in [54].

3.1 Introduction

Luminous Red Galaxies (LRGs) are one of the old and very luminous populations of galaxies in the Universe. The gas of these galaxies having being turned into stars a long time ago, there is typically very little star formation occurring today. The remainder of the stellar population is primarily old red stars, which give these galaxies their name. The spectra of LRGs are characterized by the presence of the 4000Å break, shown in fig.(3.1). For this reason the redshift of LRGs can be estimated with good accuracy ($2-5\%$) from their colors only, without taking a spectrum.

Most LRGs live in massive dark matter halos and often they are found at the center of these halos [60]. As a result they are good tracers of the underlying dark matter with a large bias (b) relative to the underlying density distribution. Any features of the dark matter power spectrum will be observed in the LRGs power spectrum amplified by the b^2 factor appropriate for LRGs. For galaxies where b is small, we need a high number density to resolve these features. However, for galaxies where b is large, as in the case of LRGs, we need a relatively small number

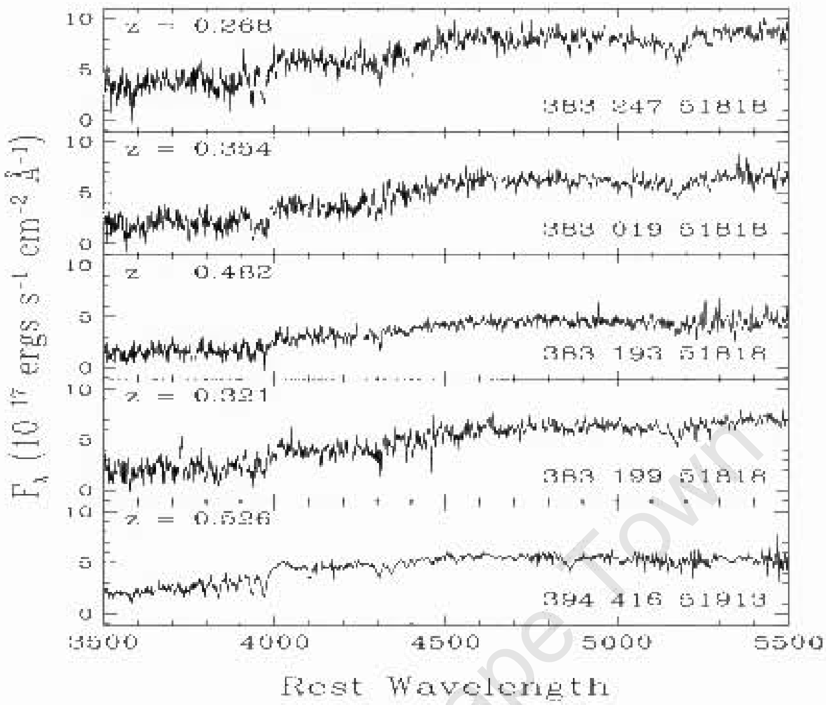

FIGURE 3.1: Spectra of 5 LRG, with the wavelengths shifted to the rest-frame. The first three spectra illustrate a progression of redshift, the fourth spectrum shows a mild emission line, and the last spectrum shows extra Balmer absorption. The latter two phenomena occur only rarely in the sample of the SDSS LRGs [59]. We can clearly see the distinct features of the 4000Å break in all the spectra. This figure is taken from Eisenstein et. al. [59]

density. This is one important advantage that LRG surveys have over other galaxy type surveys.

3.1.1 The Sloan Digital Sky Survey (SDSS)

The SDSS is an imaging and spectroscopic survey with a dedicated optical 2.5 meter telescope. The camera consists of 30 2048 × 2048 mosaic CCDs positioned in six columns and five rows [61]. The telescope is located in the Apache Point Observatory in New Mexico. It has a field of view of $3 \times 3deg^2$ with a spatial scale of $0.4''pix^{-1}$ in five passbands (u, g, r, i, z) with central wavelengths 3560, 4680, 6180, 7500 and 8870 Å respectively [62]. The primary goals of the survey are to obtain imaging of $10,000deg^2$ of the North Galactic Cap in all of five bands, spectroscopic redshifts of 10^6 galaxies and 10^5 quasars. The spectra of objects

University of Cape Town

are obtained by a multi-object spectrograph, which has a capability of taking 640 spectra at once. The wavelength range of each spectrum is 3800-9200 Å [63].

The latest public data release of the SDSS at the time of writing is the Data Release 7 (DR7) [64]. This release consists of a total area of 11663 deg^2 and contains images and parameters of 357 million objects over this area. The DR7 spectroscopic data covers 7500 deg^2 with a total number of 1.6 million spectra. The contributions of galaxies, Quasars, and other types (eg. stars, sky-spectra, unknowns) to this number are 930,000, 120,000, 460,000, respectively [64],[*www.sdss.org*].

3.2 The MegaZ-LRG Catalogue

University of Cape Town

The MegaZ-LRG catalogue [58] is a photometric catalogue of LRGs extracted from SDSS imaging samples. The redshifts of the galaxies in the catalogue span $0.4 - 0.7$ with a number distribution of galaxies on the sky shown in Fig. (3.2).

3.2.0.1 Selection Criteria

The selection of the LRGs in the redshift range of $0.4 < z < 0.7$ is done by using a series of color and magnitude cuts. The cuts are designed in such a way that they match the spectroscopic LRG data from the 2SLAQ survey which provide the training data for the Artificial Neural Networks (ANNs). [58]

When the galaxies are plotted in a color-color (g-r, r-i) diagram, galaxies in the main sample and the LRGs lie in separate regions of the diagram. This provides a first list of potential LRG candidates. However, since M-type stars have also very similar *gri* colors to the LRGs, color and magnitude cuts cannot remove them completely. In the 2SLAQ survey these stars are discriminated from their spectra. Since we don't have the spectra for the photometric data, the MegaZ data will have a contamination from these stars. The contamination, however, is minimized by using the ANNs which uses all of the photometry data to produce a star-galaxy probability that reduces the contamination to 2% [58].

FIGURE 3.2: Density map of DR4 LRGs in the SDSS footprint for the redshift bin $z \approx 0.45 - 0.50$. Most of the galaxies in the MegaZ catalogue are found in this redshift bin. We used the HEALpix [65] pixlization scheme with nside=128.

University of

3.2.0.2 The MegaZ Window Function

The SDSS angular region that the DR4 (Data Release 4) MegaZ catalogue covered is $110^\circ < \alpha < 270^\circ$ in right ascension and $-5^\circ < \delta < 70^\circ$ in declination. The south galactic plane (stripes 76, 82, and 86) are excluded as they contribute small numbers of galaxies and are widely spaced from the rest of the survey region [54, 58].

The window function for the MegaZ catalogue is constructed by assigning a "1" for each observed pixel of the sky and a "0" otherwise. The resulting surveyed area is $5,914deg^2$ with a total volume of $2.5h^{-3}Gpc^3$ across the redshift range of $0.4 < z < 0.7$.

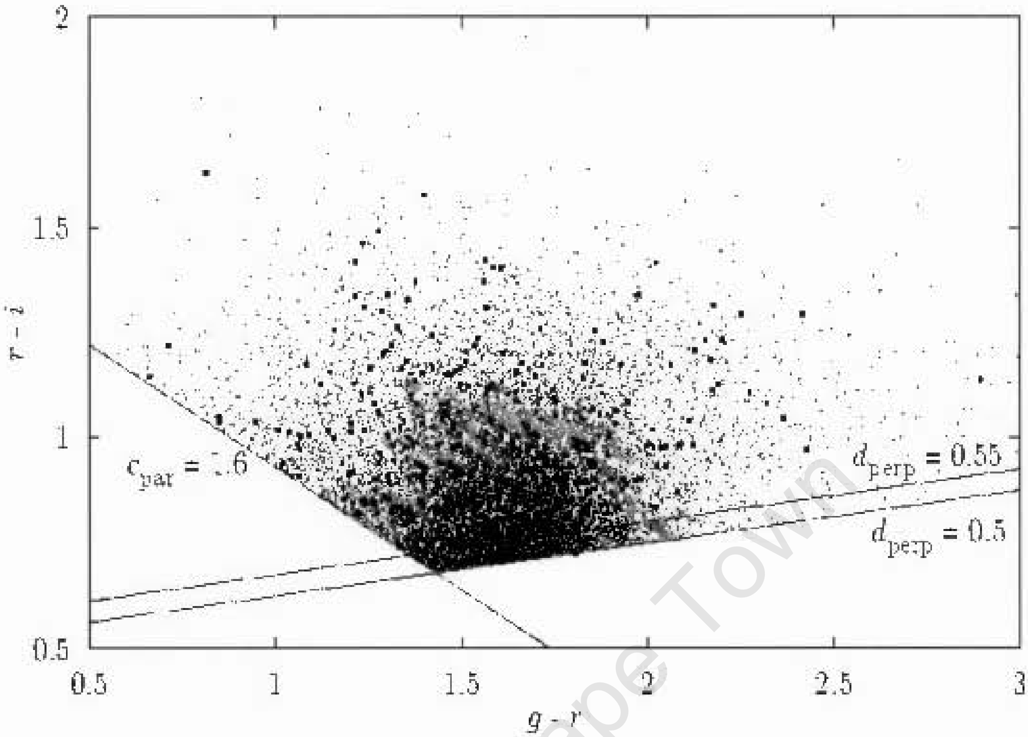

FIGURE 3.3: Colour distributions of 2SLAQ LRGs (squares) and MegaZ-LRG targets (small points). The selection on $c_{par} = 0.7(g - r) + 1.2(r - i - 0.18) > 1.6$ separates later-type galaxies from the LRG sample while cuts above lines of constant $d_{perp} \equiv (r - i) - (g - r)/8.0 > 0.5$ select early-type galaxies with increasingly high redshift. $g - r$ and $r - i$ in d_{perp} and c_{par} are colors defined by the photometric bands of the SDSS. This figure is taken from Collister et al. [58]

University of Cape Town

There are different effects that can potentially distort the window function away from the binary coverage map [66]. These include dust extinction, seeing variations, incompleteness in the vicinity of very bright stars or galaxies, and systematic effects induced by star-galaxy separation [54]. It is shown in [54] that a partial sky observation leads to the correlation of adjacent modes in the power spectrum or any other clustering statistics and hence one needs to bin adjacent modes over a sufficiently large window to remove the correlations. We bin over $\Delta\ell = 10$ as we will discuss later in detail.

3.2.0.3 Photometric Redshifts

The redshifts of the MegaZ LRGs are obtained by using the Artificial Neural Network package known as ANNz [58, 67]. Artificial neural networks are mathematical models that simulate the human neural networks in the brain and learn the relations between input and output parameters by optimizing the weight of each neuron. The ANNz package used to produce the MegaZ catalogue was first developed by [67]. It was trained by spectroscopic data from 2SLAQ and SDSS to predict the redshift of a galaxy from its photometric data. The basic inputs in the training are therefore the five band colors and the spectroscopic redshift.

The ANNz root mean square error for predicting the redshift of the photometric LRGs was found to be [58]:

$$\delta z_{phot} \approx 0.041 \tag{3.1}$$

This accuracy is independent of any systematic error in the spectroscopic training redshifts. The accuracy of the photometric redshift prediction reaches the 2% level for the brightest LRGs. Fig.(3.4) shows the dispersion of the photometric redshifts predicted by the ANNz for the spectroscopic data.

We follow Blake et al. [54] by binning the MegaZ catalogue in four photometric redshift slices of width $\Delta z = 0.05$ from $z = 0.45$ to $z = 0.65$. Because of the uncertainty in the photometric redshift, there is a finite chance that galaxies whose redshift are close to the bin edge end up in the wrong bin. This will cause a non diagonal covariance matrix between different redshift bins and therefore one needs to compute the full covariance matrix before combining statistical results from the different bins.

The redshift distribution of LRGs across each bin in the MegaZ catalogue is well fit by a Gaussian curve fig.(3.6).

3.3 Angular Power Spectrum and Bispectrum of the MegaZ Catalogue

In the previous chapter we introduced the equations for the angular power spectrum and bispectrum. Before applying them to the MegaZ catalogue, we carried out a number of tests that check the validity of these equations and our codes.

University of Cape Town

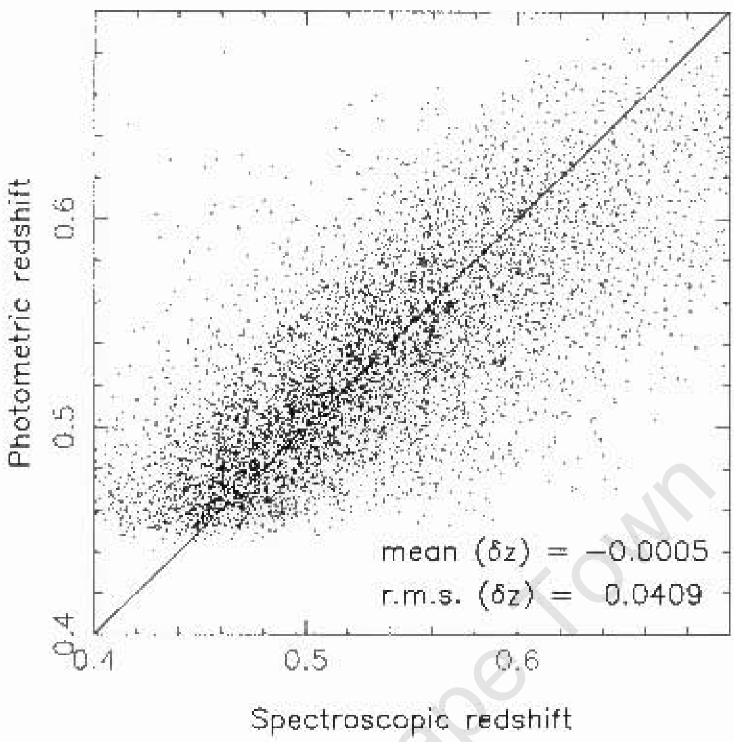

FIGURE 3.4: Dispersion of the photometric redshift determined by ANNz. The spectroscopic redshifts are from 2SLAQ and SDSS. The r.m.s error on the photometric redshift ($\delta z = z_{phot} - z_{spec}$) are indicated. This figure is taken from Blake et al. [54]

First we computed the power spectrum and bispectrum for a large set of uniformly distributed points across the whole sky using a Monte Carlo (MC) method. We then checked the partial sky case which was selected to have an similar RA and Dec range as that of the MegaZ catalogue. Since both the power spectrum and bispectrum vanish for a uniform distribution, we demanded that our code recovered $A_{lm} = 0$ (when shot noise is subtracted). We also showed the validity of the error approximations for C_l and $B_{l_1 l_2 l_3}$ by comparing the theoretical estimates of the error with the error calculated from many realizations.

Details of these tests are given in Appendix A.1 which show that the A_{lm} and error estimators given in Eqs.(2.32, 2.33, 2.26) are very good approximations. Hence, for the rest of this thesis we will use these equations to compute the power spectrum and bispectrum of the MegaZ-LRG catalogue.

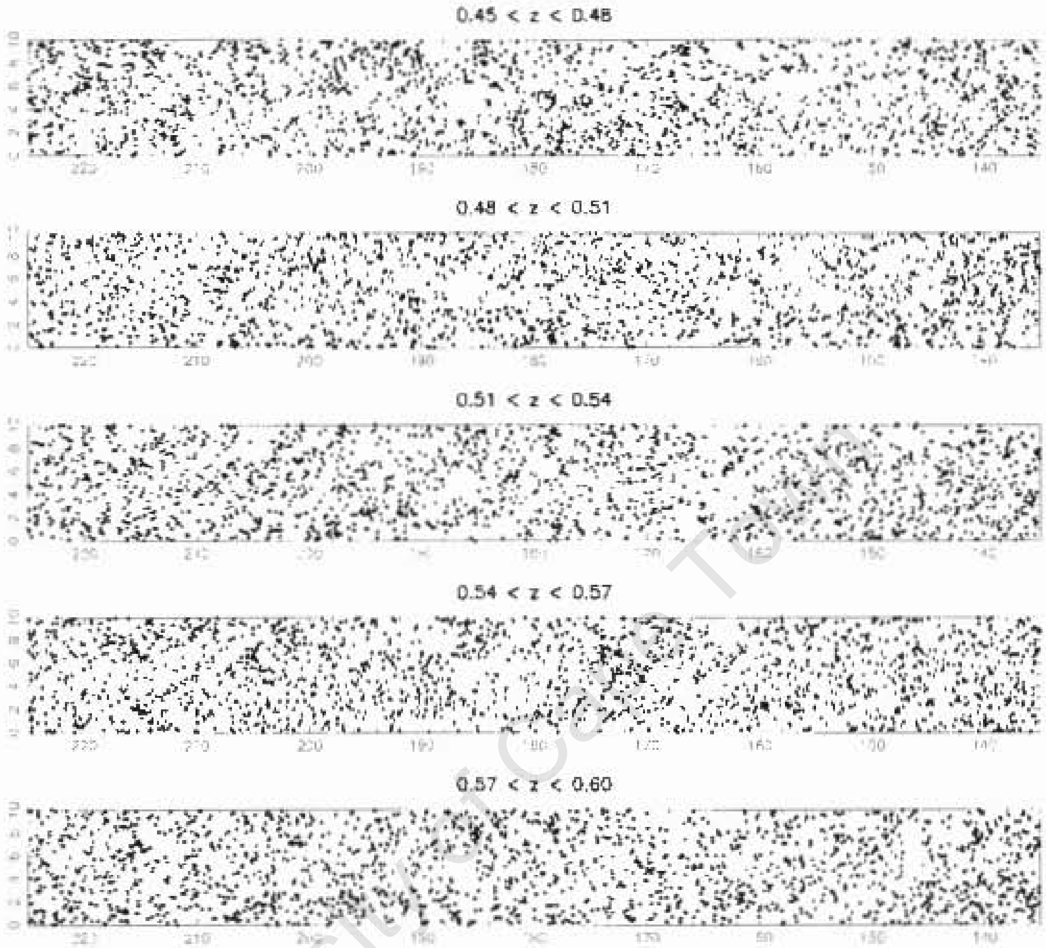

FIGURE 3.5: The locations of the 2000 most luminous galaxies in each of a series of photometric redshift slices of width $\Delta z = 0.03$ in a narrow survey stripe. The characteristic patterns of large-scale structure may be observed. The axes are right ascension and declination in decimal degrees. This figure is taken from Blake et al. [54].

University of Cape Town

3.3.1 The Angular Power Spectrum of the MegaZ Catalogue

A detailed analsis of the angular power spectrum for the DR4 release of MegaZ-LRG catalogue has been done by [54]. In this section we review some of their key results and reproduce their angular power spectrum plots as an additional test of our code.

In their paper Blake et al. [54] showed that

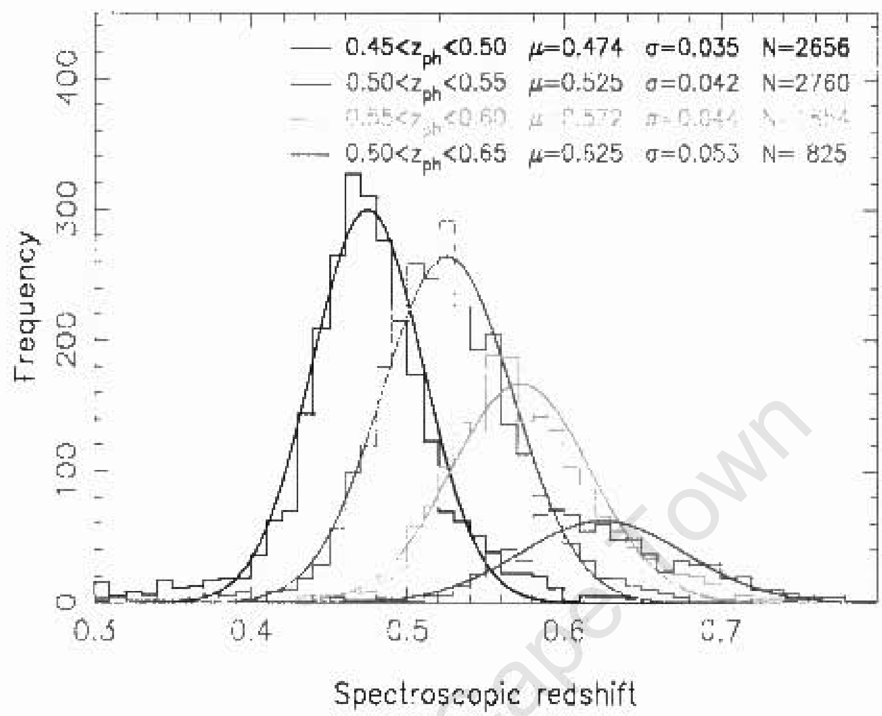

FIGURE 3.6: Redshift selection function of the MegaZ-LRGs for each of the four redshift slices in the range $z = 0.45$ to $z = 0.7$. We can clearly see that the selection function in each bin is well fit by a Gaussian curve. The best fitting Gaussian parameters μ, σ and the number of galaxies at each redshift slice are indicated at the top right corner of the plot. The fitting equation is: $p(z) = \frac{1}{\sqrt{2\pi\sigma^2}}\left[\exp\left(\frac{-(z-\mu)^2}{2\sigma^2}\right)\right]$. [54]

University of Cape Town

- The correlation between adjacent multipoles of the angular power spectrum caused by the window function of the MegaZ region drops to 10% from its peak for $\Delta l \simeq 10$. Therefore one can safely assume, at the 10% level, that the cooresponding bands of the angular power spectrum are independent for $\Delta\ell = 10$

- The statistical error on the angular power spectrum in the quasi-linear regime can be approximated by the following formula

$$\sigma(C_l) = \sqrt{\frac{2}{f_{sky}(2l+1)}}\left(C_l + \frac{1}{N/\Delta\Omega}\right). \tag{3.2}$$

where $\Delta\Omega$ is the area of the sky observed, in this case $5,914deg^2$, $f_{sky} = \frac{\Delta\Omega}{4\pi}$ is the fractional area of the sky observed and N is the number of galaxies. The

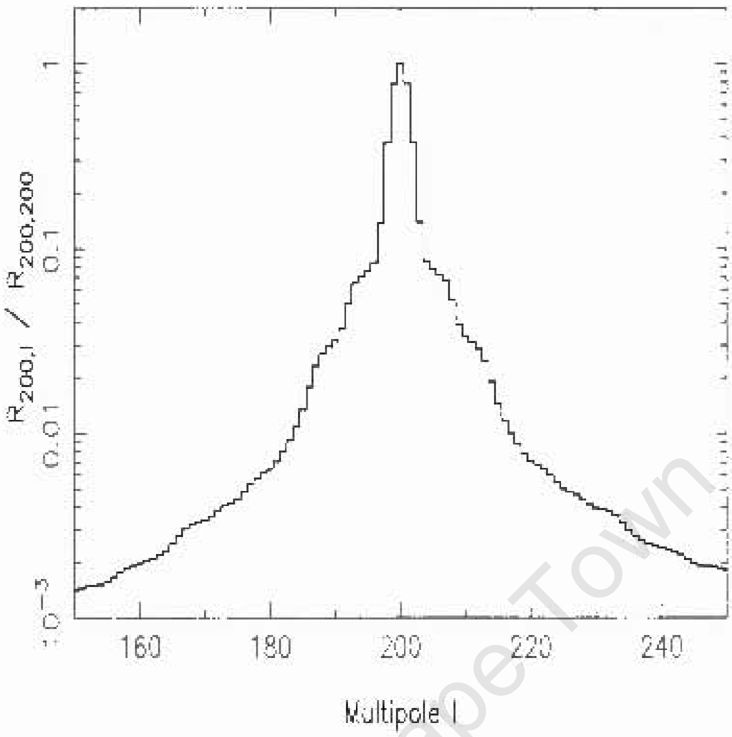

FIGURE 3.7: The mixing matrix $R_{\ell\ell}$ for multipole $\ell = 200$ as a function of ℓ, indicating the range of multipoles correlated by the survey window function effects. The range of multipoles correlated by the window function drops very rapidly. For $\Delta l = 10$, the correlation is less than 10%. This figure is taken from Blake et al. [54].

University of Cape Town

two terms on the right hand side of the above equation are contributions from cosmic variance (C_l) and shot noise $[(N/\Delta\Omega)^{-1}]$ respectively. The $1/(2l+1)$ factor is due to the average over spherical harmonic index m. The effect of the survey window function is encapsulated by the $1/\sqrt{f_{sky}}$ factor. Eq.(2.32) is further divided by $\sqrt{\Delta\ell}$ to account for the binning of the multipoles which is necessary to minimize the correlations between adjacent modes.

- The best fit cosmological parameter values for the angular power spectrum of the MegaZ catalogue over the series of redshift slices are given by $\Omega_m \approx 0.27$, $\frac{\Omega_b}{\Omega_m} \approx 0.17$, $H_0 = 75kms^{-1}Mpc^{-1}$ and $n_s = 1$. When combining the different redshift slices with the appropriate covariance matrix the constraints on the cosmic parameters for fixed values of H_0, and n_s while marginalizing over σ_8 and bias are $\Omega_m h = 0.195 \pm 0.023$, $\frac{\Omega_b}{\Omega_m} \approx 0.16 \pm 0.04$. These constraints are similar in precision to those of the constraints from spectroscopic data [68]. Blake et al. in their paper concluded that photometric redshift surveys are

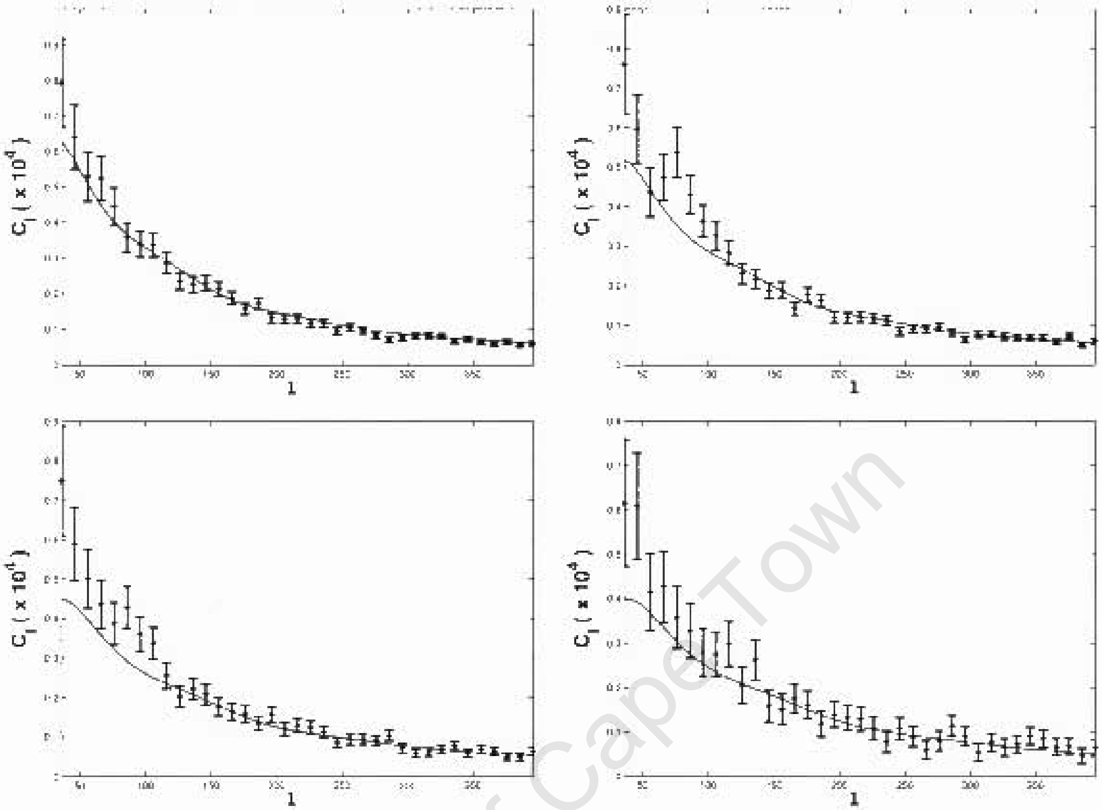

FIGURE 3.8: The angular power spectrum of the MegaZ-LRGs together with the theoretical curve for the best fitting parameter values, $\Omega_m = 0.27$, $\frac{\Omega_b}{\Omega_m} = 0.17$, $H_0 = 75kms^{-1}Mpc^{-1}$, $n_s = 1$ and $\sigma_8 = 1$. The different figures are, the 1^{st} redshift bin, $0.45 < z \leq 0.5$, (top left), the 2^{nd} redshift bin, $0.5 < z \leq 0.55$, (top right), 3^{rd} redshift bin, $0.55 < z \leq 0.6$, (bottom left) and the 4^{th} redshift bin, $0.6 < z \leq 0.65$, (bottom right). The values of the linear bias parameters used are $b = 1.51$, $b = 1.68$, $b = 1.74$ and $b = 1.95$ for the 1^{st}, 2^{nd}, 3^{rd} and 4^{th} redshift bins respectively. To avoid correlation between adjacent multipoles, the C_l's are binned over $\Delta l = 10$

University of Cape Town

competitive with spectroscopic surveys for the measurement of cosmological parameters in the simple "vanilla" model. This is because of the large number of galaxies in the photometric surveys.

- The DR4 MegaZ photo-z catalogue has shown a visual hint of the baryon acoustic oscillations despite its significance level being less than 3σ.
- The photometric systematics in the MegaZ catalogue have no significant effect on the angular power spectrum.

In fig.(3.8) we show our results for the angular power spectrum which agrees very well with those of Blake et al. [54].

University of Cape Town

Chapter 4

Non-Gaussianity of the MegaZ-LRG Catalogue

University of Cape Town

In this chapter we present the main results of this thesis by dividing in two parts: first we discuss the angular bispectrum followed by the implications of the bispectrum for the primordial non-Gaussianity parameter f_{NL}.

4.1 MegaZ Catalogue Angular Bispectrum

To calculate the bispectrum for the MegaZ catalogue, we first computed the partial sky estimator of the spherical harmonic coefficients, a_{lm} given by [54]:

$$A_{lm} = \sum_{\theta,\phi} Y_{lm}(\theta, \phi) - \sigma_0 I_{lm} \,, \tag{4.1}$$

where σ_0 is the surface density and the geometry term I_{lm} is given by

$$I_{lm} = \int_{\Delta\Omega} Y^*_{lm} d\Omega \,. \tag{4.2}$$

$\Delta\Omega$ is the area of the sky that is observed. We used Monte Carlo integration to compute this integral. Since it depends only on the angular coverage, we use the same I_{lm} for all the redshift bins.

Once we compute the A_{lm}'s for the MegaZ data points, we multiply triplets of them according to Eq.(2.29) for the different choice of triangles, specified by sides

ℓ_1, ℓ_2 and ℓ_3, to get the angle-averaged bispectrum. The choice of independent triangles is controlled by the Wigner-3j symbols, which will ensure that the three conditions listed just after Eq.(2.29) are satisfied. Therefore we loop over ℓ_1, ℓ_2, ℓ_3, up to $\ell_{\max} \sim 200$, which is roughly the limit of the quasi-linear regime for the mean MegaZ galaxy redshift. Later we will show the sensitivity of our result as we vary $\ell_{\max}$. The error on the bispectrum estimate is calculated by using the theoretical approximation given by Eq.(2.33).

Since adjacent multipoles are correlated due to the window function, we binned the multipoles with $\Delta\ell = 10$ for each of ℓ_1, ℓ_2, ℓ_3. As discussed in the previous chapter this allows us to treat each multipole bin as independent. We use an inverse variance weight scheme (IVWS) to do the averaging in all the bins. The equation that describes this averaging scheme is then given by:

$$B_{l_1 l_3 l_3} = \frac{\sum_{\Delta\ell_i} W_{l_1 l_2 l_3} \tilde{B}_{l_1 l_2 l_3}}{\sum_{\Delta\ell_i} W_{l_1 l_2 l_3}} \tag{4.3}$$

$$\sigma(B_{l_1 l_3 l_3}) = \left(\sum_{\Delta\ell_i} W_{l_1 l_2 l_3} \right)^{-\frac{1}{2}} \tag{4.4}$$

where $i = 1, 2, 3$ and the weight $W_{l_1 l_2 l_3} = \sigma(\tilde{B}_{l_1 l_2 l_3})^{-2}$ and $\sigma(\tilde{B}_{l_1 l_2 l_3})$ is the error on the unbinned bispectrum which is given by Eq. (2.33)

Fig.(4.4) shows the angle-averaged bispectrum of the DR4 MegaZ catalog with the multipoles binned over bands of $\Delta\ell = 10$ for the different redshift bins and a variety of triangular configurations.

4.2 Extracting the Primordial Non-Gaussianity, f_{NL}

The main sources of non-Gaussianity in the large scale structure are Primordial non-Gaussianity, non-linear gravitational collapse during structure formation, and galaxy bias relative to the underlying dark matter. The contribution of these non-Gaussianities in the bispectrum are distinct and hence we can treat them independently and disentangle their effects.

University of Cape Town

As we have discused in the earlier chapters, we will characterize primordial non-Gaussianity by writing the gravitational potential as

$$\Phi = \Phi_L + f_{NL}\left[\Phi_L^2 - \langle\Phi_L^2\rangle\right] \,. \tag{4.5}$$

The non-Gaussianity that we are dealing with by using this form for Φ is of a local type. In these models the signal for the bispectrum comes mainly from the squeezed triangular configurations, $k_1 \ll k_2, k_3$. It is shown in [40] that the local and non-local types will have the same form when one considers the equilateral triangular configuration ($\ell_1 = \ell_2 = \ell_3$).

The 3D bispectrum in Fourier space resulting from the above expansion of the gravitational potential is given by [40]

$$B_\Phi(k) = 2f_{NL}[P_\Phi(k_1)P_\Phi(k_2) + \text{cyc.}] \tag{4.6}$$

where $P_\Phi(k)$ is the primordial power spectrum and "cyc" denotes cyclic permutations of k_1, k_2, k_3.

The matter density field is related to the primordial gravitational potential through Poisson's equation [48], $\delta(k,z) = M(k,z)\phi(k)$, where

$$M(k,z) = \frac{2}{3}\frac{k^2T(k)(1+z)D(z)}{\Omega_m H_0^2} \,. \tag{4.7}$$

Here $T(k)$ is the matter transfer function, $D(z)$ is the growth function, and H_0 and Ω_m are the Hubble parameter and fractional matter density today, respectively. [1]

The bispectrum from this matter density field is then given by

$$\begin{aligned} B(k_1,k_2,k_3,z) &= \langle\delta(k_1)\delta(k_2)\delta(k_3)\rangle & (4.8)\\ &= M(k_1,z)M(k_2,z)M(k_3,z)B_\phi(k) & (4.9) \end{aligned}$$

[1]The definition of $M(k,z)$ we use in this thesis is the same as that in [40]

University of Cape Town

which can be rewritten as

$$\begin{aligned} B(k_1,k_2,k_3,z) &= 2f_{NL}(P_L(k_1,z)P_L(k_2,z)\frac{M(k_3,z)}{M(k_1,z)(k_2,z)} \\ &\quad + P_L(k_1,z)P_L(k_3,z)\frac{M(k_2,z)}{M(k_1,z)(k_3,z)} \\ &\quad + P_L(k_2,z)P_L(k_3,z)\frac{M(k_1,z)}{M(k_2,z)(k_3,z)}) . \end{aligned} \tag{4.10}$$

Since we are working in harmonic space for the MegaZ catalogue, we need to project Eq.(4.10) into the spherical harmonic space. Projecting the bispectrum looses information and decreases the number of triplets we can consider. However, in our case the signal to noise ratio of the bispectrum will still be strong due to the narrow width of the redshift slices and the large number density of galaxies in the MegaZ catalogue. We do the projection of the full 3D Fourier space bispectrum into 2D spherical harmonics by using the Limber approximation [69, 70], which is good for small angular scales. The final equation that we will be using to constrain the non-Gaussianity parameter f_{NL} from the MegaZ-LRG catalogue is therefore written as [57]

$$B_{l_1 l_2 l_3} \approx \begin{pmatrix} l_1 & l_2 & l_3 \\ 0 & 0 & 0 \end{pmatrix} \sqrt{\frac{(2l_1+1)(2l_2+1)(2l_3+1)}{4\pi}} B(l_1,l_2,l_3) \tag{4.11}$$

where

$$B(l_1,l_2,l_3) = f_{NL}\int_{\chi_i}^{\chi_f} d\chi \left(p(z)\frac{dz}{d\chi}\right)^3 \frac{1}{\chi^4} B\left(\frac{l_1}{\chi},\frac{l_2}{\chi},\frac{l_3}{\chi},z\right) \tag{4.12}$$

where $p(z)$ is the redshift selection function and χ is the co-moving radial distance. To obtain a constraint on primordial non-Gaussianity we consider five types of triangular configurations:

1. $\ell_1 = \ell_2 = \ell_3 = \ell$ equilateral configuration
2. $\ell_1 = \ell_2 = \ell; \ell_3 = 2\ell$ degenerate configuration
3. $\ell_1 = \ell; \ell_2 = 2\ell; \ell_3 = 3\ell$ squeezed configuration
4. $\ell_1 = \ell; \ell_2 = 4\ell; \ell_3 = 5\ell$ squeezed configuration
5. $\ell_1 = \ell; \ell_2 = 5\ell; \ell_3 = 6\ell$ squeezed configuration

University of Cape Town

These choices are somewhat arbitrary and are meant only to be representative of the interesting triangles for the local (squeezed) and non-local (equilateral) models. We also summed over all the possible triangular configurations in the range $\ell_{\min} < \ell_1 < \ell_2 < \ell_3 < \ell_{\max}$. We use $\ell_{\min} = 20$ due to the limitation of the small angle approximation and $\ell_{\max} = 200$ due to the limit of the quasi-linear region. This provides a total χ^2 which is simply the sum of the individual χ^2's for each triangular configuration [24].

4.2.1 Main Results

In this section we present the final constraints on f_{NL} from the DR4 version of the MegaZ catalogue. Because of the different redshift bins and triangular configurations there are a large number of constraints which are summarized in Tables (4.1 - 4.4) .

The best-fitting theoretical bispectra are shown against the data in Figures (4.1 - 4.4). To derive our constraints we use the χ^2 statistic to find the best fitting value for f_{NL} in Eq.(4.11). The χ^2 statistic is defined as:

$$\chi^2(f_{NL}) = \sum_{\ell_{\min}}^{\ell_{\max}} \frac{(B^{\rm Data}_{\ell_1\ell_2\ell_3} - f_{NL} B^{\rm Theory}_{\ell_1\ell_2\ell_3})^2}{\sigma^2_{B_{\ell_1\ell_2\ell_3}}} \tag{4.13}$$

where we typically choose $\ell_{\min} = 20$ and $\ell_{\max} = 200$ to be conservative. This expression is minimized to find the best-fit value of f_{NL}. Fig.(4.5) shows the χ^2 as a function of f_{NL} for the sum over all triangular configurations of the first redshift bin in the MegaZ catalogue. To derive confidence limits we assume that the χ^2 statistic is quadratic in f_{NL} and hence the 1,2, and 3 σ confidence limits correspond to the distance from the best fitting f_{NL} to those values of f_{NL} for which the χ^2 is 1,4 and 9 larger than the minimum value of χ^2 respectively. Since the theoretical predictions are linear in f_{NL} the Fisher matrix errors are exact and the χ^2 is quadratic in f_{NL}, as can be seen in Fig.(4.5).

Many are consistent with $f_{NL} = 0$ in Tables (4.1 - 4.4). However there are several notable exceptions. The $\ell_1 = \ell_2, \ell_3 = 2\ell_1$ configuration in the lowest redshift bin gives $(1 - \sigma$ error bars)

$$f_{NL} = 90 \pm 23 \tag{4.14}$$

University of Cape Town

which implies $f_{NL} > 0$ with nearly $4 \cdot \sigma$.

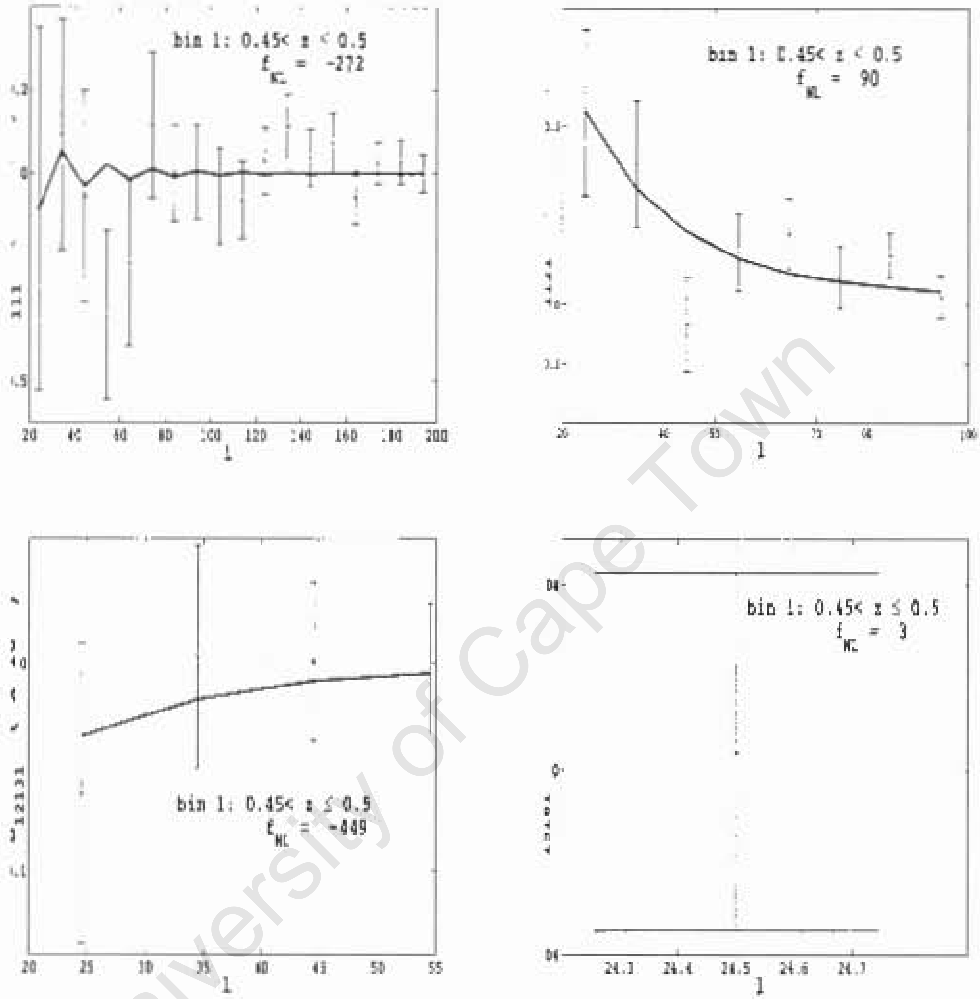

FIGURE 4.1: The angular bispectrum from the MegaZ-LRGs together with the best-fitting theoretical bispectra for the 1st redshift bin. The different figures are the bispectrum for $\ell_1 = \ell_2 = \ell_3$ (top left), $\ell_1 = \ell_2, \ell_3 = 2\ell_2$ (top right), $\ell_1, \ell_2 = 2\ell_1, \ell_3 = 3\ell_1$ (bottom left), $\ell_1, \ell_2 = 2\ell_1, \ell_3 = 3\ell_1$ (bottom right) triangular configurations. To avoid correlation between adjacent multipoles, the bispectrum values are binned in bands of $\Delta\ell = 10$.

University of Cape Town

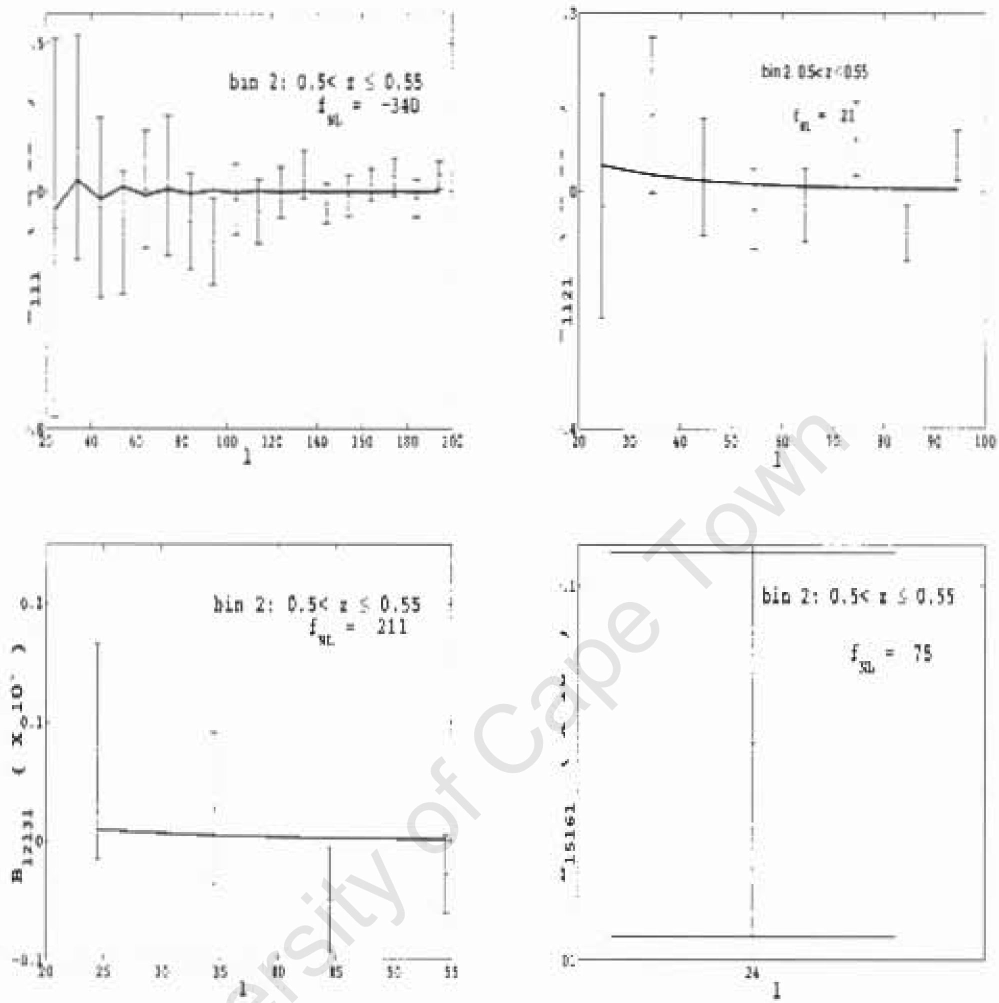

FIGURE 4.2: The angular bispectrum from the MegaZ-LRGs together with the best-fitting theoretical bispectra for the 2[nd] redshift bin. The different figures are the bispectrum for $\ell_1 = \ell_2 = \ell_3$ (top left), $\ell_1 = \ell_2, \ell_3 = 2\ell_2$ (top right), $\ell_1, \ell_2 = 2\ell_1, \ell_3 = 3\ell_1$ (bottom left), $\ell_1, \ell_2 = 2\ell_1, \ell_3 = 3\ell_1$ (bottom right) triangular configurations. To avoid correlation between adjacent multipoles, the bispectrum values are binned in bands of $\Delta\ell = 10$.

University of Cape Town

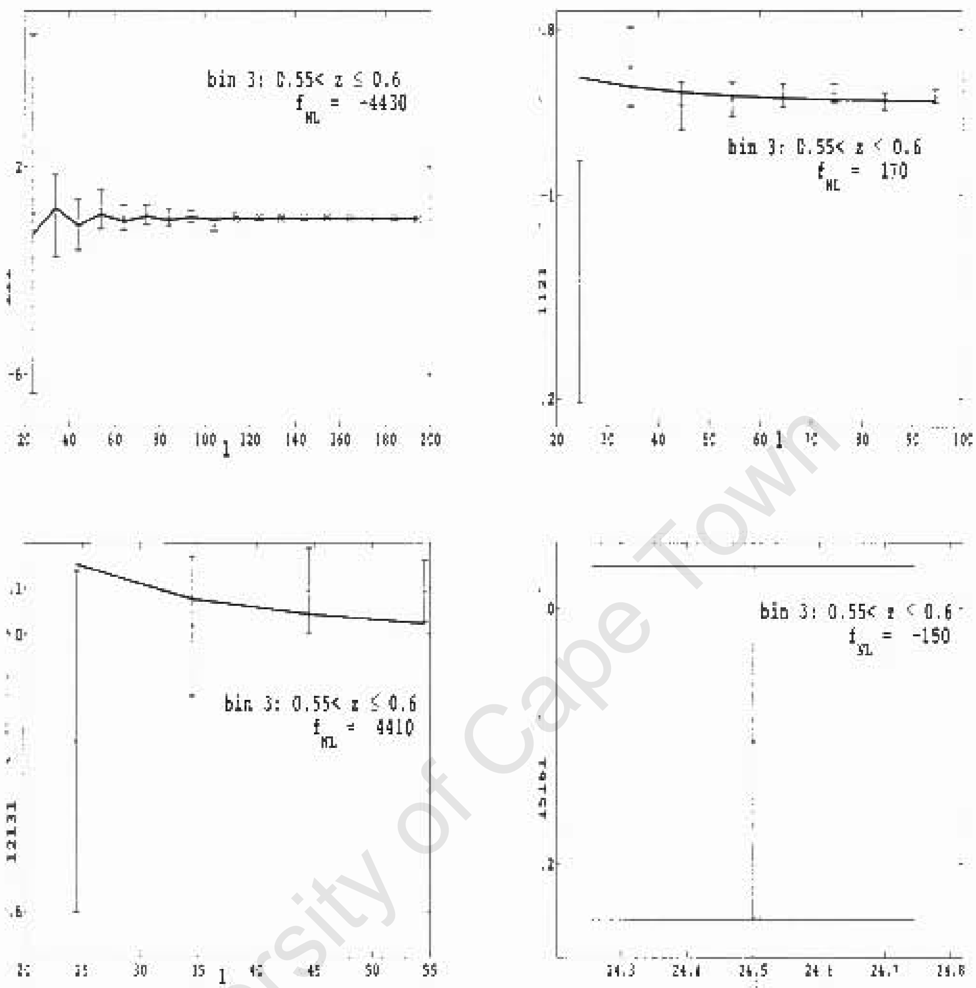

FIGURE 4.3: The angular bispectrum from the MegaZ-LRGs together with the best-fitting theoretical bispectra for the 3rd redshift bin. The different figures are the bispectrum for $\ell_1 = \ell_2 = \ell_3$ (top left), $\ell_1 = \ell_2, \ell_3 = 2\ell_2$ (top right), $\ell_1, \ell_2 = 2\ell_1, \ell_3 = 3\ell_1$ (bottom left), $\ell_1, \ell_2 = 2\ell_1, \ell_3 = 3\ell_1$ (bottom right) triangular configurations. To avoid correlation between adjacent multipoles, the bispectrum values are binned in bands of $\Delta\ell = 10$.

University of Cape Town

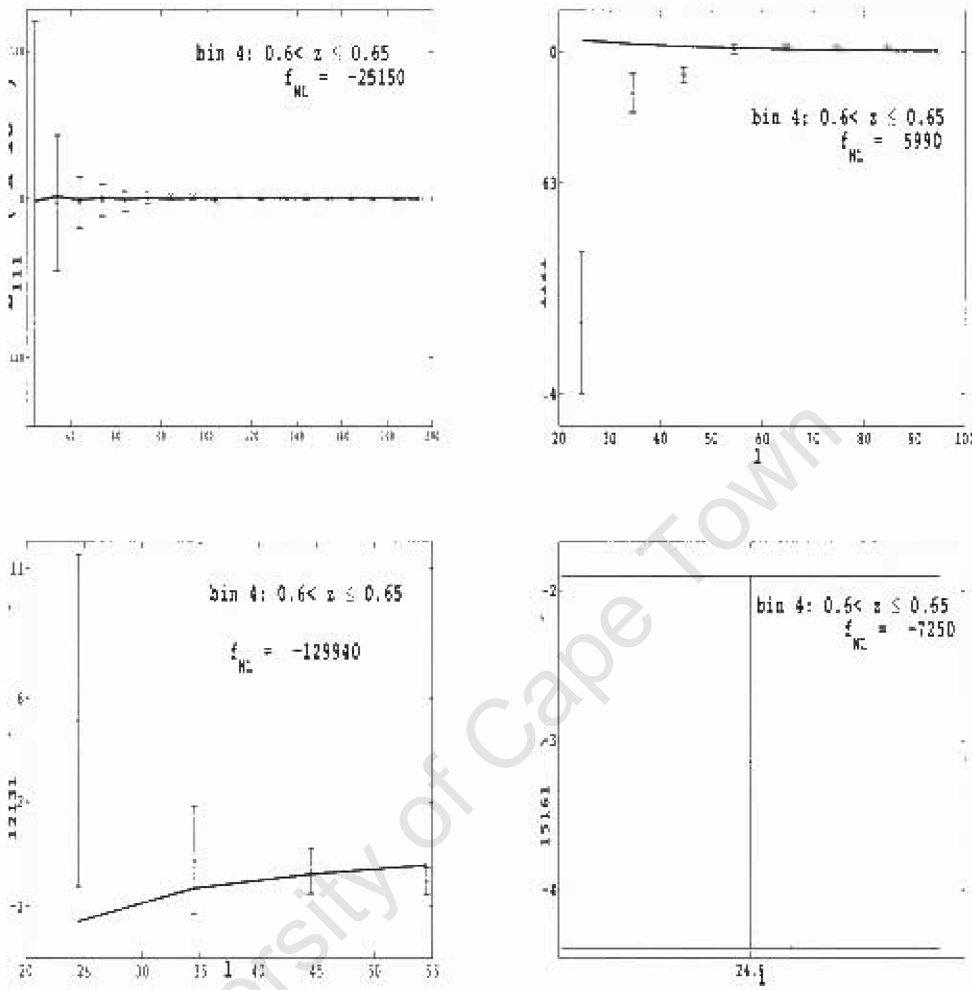

FIGURE 4.4: The angular bispectrum from the MegaZ-LRGs together with the best-fitting theoretical bispectra for the 4^{th} redshift bin. The different figures are the bispectrum for $\ell_1 = \ell_2 = \ell_3$ (top left), $\ell_1 = \ell_2, \ell_3 = 2\ell_2$ (top right), $\ell_1, \ell_2 = 2\ell_1, \ell_3 = 3\ell_1$ (bottom left), $\ell_1, \ell_2 = 2\ell_1, \ell_3 = 3\ell_1$ (bottom right) triangular configurations. To avoid correlation between adjacent multipoles, the bispectrum values are binned in bands of $\Delta\ell = 10$.

University of Cape Town

Triangle type	f_{NL} *with* 1σ *error*	*Min* χ^2	*Number of* σ *away from* $f_{NL}=0$
$\ell_1=\ell_2=\ell_3$	-272 ± 778	10.5	$0.3\ \sigma$
$\ell_1=\ell_2;\ \ell_3=2\ell_1$	90 ± 23	7.3	$3.9\ \sigma$
$\ell_1;\ \ell_2=2\ell_1;\ \ell_3=3\ell_2$	-449 ± 705	0.4	$0.6\ \sigma$
$\ell_1;\ \ell_2=4\ell_1;\ \ell_3=5\ell_1$	-1011 ± 592	0.3	$1.7\ \sigma$
$\ell_1;\ \ell_2=5\ell_1;\ \ell_3=6\ell_1$	3 ± 30	0.0	$0.1\ \sigma$

TABLE 4.1: Result for the 1st redshift slice, $0.45<z\leq0.5$. The number of LRGs in this bin is $N=211263$. The minimum and maximum ℓ's considered here are $\ell_{\rm min}=20$ and $\ell_{\rm max}=200$.

The other non-trivial triangular configuration in the first redshift bin is the $\ell_1,\ell_2=4\ell_1,\ell_3=5\ell_1$ which yields $f_{NL}=-1011\pm592$ with 68% CL. In contrast to the constraint in Eq. (4.14), this gives $f_{NL}<0$ at nearly $2-\sigma$ confidence.

Although the number of galaxies in the high-z bin (the fourth redshift bin) is small, we found two $2.5-\sigma$ positive and negative deviations from $f_{NL}=0$. The $\ell_1=\ell_2,\ell_3=2\ell_1$ triangular configuration, which gives a nearly $4-\sigma$ positive f_{NL} in the first redshift bin, yields $f_{NL}=5990\pm2385$ with 68% CL in this redshift bin; and the $\ell_1,\ell_2=5\ell_1,\ell_3=6\ell_1$ triangular configuration gives a $2.5-\sigma$ negative non-Gaussianity, $f_{NL}=-7250\pm2863$ with 68% CL.

If instead we sum over all triangular configurations, the same low-z bin gives a constraint of ($1-\sigma$ error bar)

$$f_{NL}=57\pm52 \tag{4.15}$$

which is consistent with vanishing primordial non-Gaussianity. Given the specific triangle constraints of Table 4.1, this result can be be explained from the fact that we have a conflicting result of a $4-\sigma$ positive value of f_{NL} and that of the 2-σ negative values. However, this is an ad-hoc explanation and hence we need to carry out a detailed analysis to confirm whether this is the case or not. We leave the confirmation and investigation of the origin of these results for future work.

How do these results compare with other constraints in the literature? As we discussed in section 1.3.4, the current best constraints on f_{NL} come from the WMAP data which are (95% CL): $14<f_{NL}<147$ from Yadav and Wandelt [19], from 3-year WMAP data; $-9<f_{NL}<111$ from Komatsu *et al.* [18], 5-year WMAP data; and $-4<f_{NL}<80$ from Smith *et al.* [20], 5-year WMAP data.

University of Cape Town

Triangle type	f_{NL} *with* 1σ *error*	*Min* χ^2	*Number of* σ *away from* $f_{NL} = 0$
$\ell_1 = \ell_2 = \ell_3$	-340 ± 1635	6.1	$0.2\ \sigma$
$\ell_1 = \ell_2;\ \ell_3 = 2\ell_1$	21 ± 46	7.4	$0.5\ \sigma$
$\ell_1;\ \ell_2 = 2\ell_1;\ \ell_3 = 3\ell_2$	211 ± 1448	2.8	$0.1\ \sigma$
$\ell_1;\ \ell_2 = 4\ell_1;\ \ell_3 = 5\ell_1$	-1697 ± 1187	0.1	$1.4\ \sigma$
$\ell_1;\ \ell_2 = 5\ell_1;\ \ell_3 = 6\ell_1$	75 ± 56	0.0	$1.3\ \sigma$

TABLE 4.2: Result for the 2^{nd} redshift slice, $0.5 < z \leq 0.55$. The number of LRGs in this bin is $N = 172413$. The minimum and maximum ℓ's considered here are $\ell_{\text{min}} = 20$ and $\ell_{\text{max}} = 200$.

Triangle type	f_{NL} *with* 1σ *error*	*Min* χ^2	*Number of* σ *away from* $f_{NL} = 0$
$\ell_1 = \ell_2 = \ell_3$	-4430 ± 5625	2.8	$0.8\ \sigma$
$\ell_1 = \ell_2;\ \ell_3 = 2\ell_1$	170 ± 153	4.5	$1.1\ \sigma$
$\ell_1;\ \ell_2 = 2\ell_1;\ \ell_3 = 3\ell_2$	4410 ± 5028	2.6	$0.9\ \sigma$
$\ell_1;\ \ell_2 = 4\ell_1;\ \ell_3 = 5\ell_1$	1580 ± 4088	0.0	$0.4\ \sigma$
$\ell_1;\ \ell_2 = 5\ell_1;\ \ell_3 = 6\ell_1$	-150 ± 200	0.0	$0.8\ \sigma$

TABLE 4.3: Result for the 3^{rd} redshift slice, $0.55 < z \leq 0.6$. The number of LRGs in this bin is $N = 111100$. The minimum and maximum ℓ's considered here are $\ell_{\text{min}} = 20$ and $\ell_{\text{max}} = 200$.

Triangle type	f_{NL} *with* 1σ *error*	*Min* χ^2	*Number of* σ *away from* $f_{NL} = 0$
$\ell_1 = \ell_2 = \ell_3$	-25150 ± 68264	3.7	$0.4\ \sigma$
$\ell_1 = \ell_2;\ \ell_3 = 2\ell_1$	5990 ± 2385	43.4	$2.5\ \sigma$
$\ell_1;\ \ell_2 = 2\ell_1;\ \ell_3 = 3\ell_2$	-129940 ± 91673	3.1	1.4σ
$\ell_1;\ \ell_2 = 4\ell_1;\ \ell_3 = 5\ell_1$	-62150 ± 65257	0.0	$0.9\ \sigma$
$\ell_1;\ \ell_2 = 5\ell_1;\ \ell_3 = 6\ell_1$	-7250 ± 2863	0.0	$2.5\ \sigma$

TABLE 4.4: Result for the 4^{th} redshift slice, $0.6 < z \leq 0.65$. The number of LRGs in this bin is $N = 51222$. The minimum and maximum ℓ's considered here are $\ell_{\text{min}} = 20$ and $\ell_{\text{max}} = 200$.

University of Cape Town

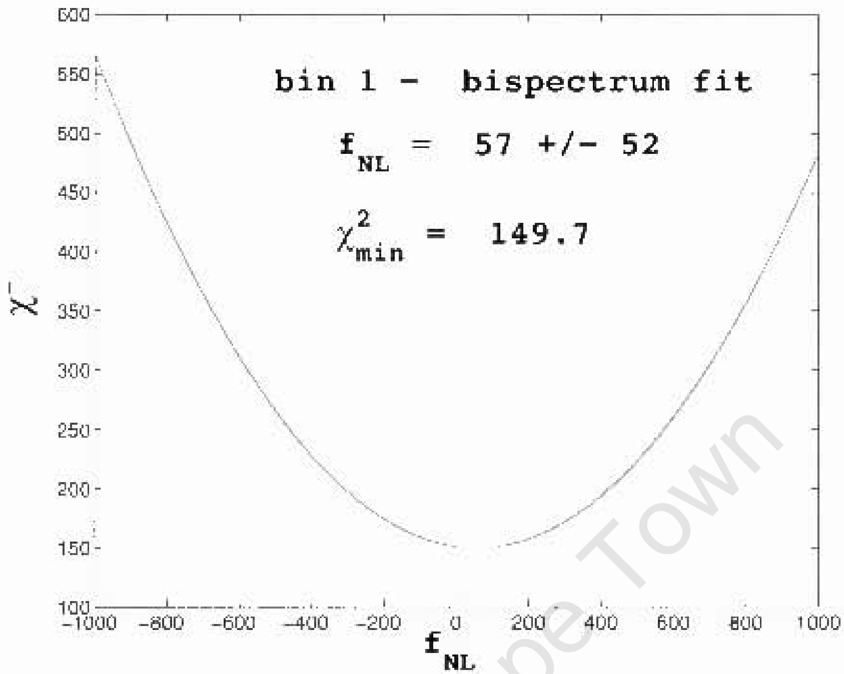

FIGURE 4.5: The χ^2 distribution as a function of f_{NL} for the first redshift bin. The χ^2 is calculated at each point in the f_{NL} grid using Eq. (4.13). We use the theory and data bispectrum from all possible triangular configurations to get this plot. As we can see from the plot the χ^2 distribution in f_{NL} is quadratic. Hence, the 1,2, and 3 σ confidence limits of the best-fitting f_{NL} correspond to the values of f_{NL} for which the χ^2 is 1,4 and 9 larger than the minimum value, respectively.

We see that our results are consistent with these results, as can be seen in Fig. (4.2.1).

University of Cape Town

4.2.2 Effect of $\ell_{\max}$ on the f_{NL} constraint

In this subsection we consider the robustness of our main results presented above as we vary $\ell_{\max}$ in Eq. (4.13). In Table (4.2.2) we show how the estimates of f_{NL} vary as we change the maximum ℓ from 200 to 400. As we can see from this table, our result is consistent across the weak non-linear regime. What this is telling us is that the signal for our result comes mainly from the large scale limit, $\ell < 200$, and hence the exclusion of the non-linear gravitational collapse from our analysis can not have a large effect on our result.

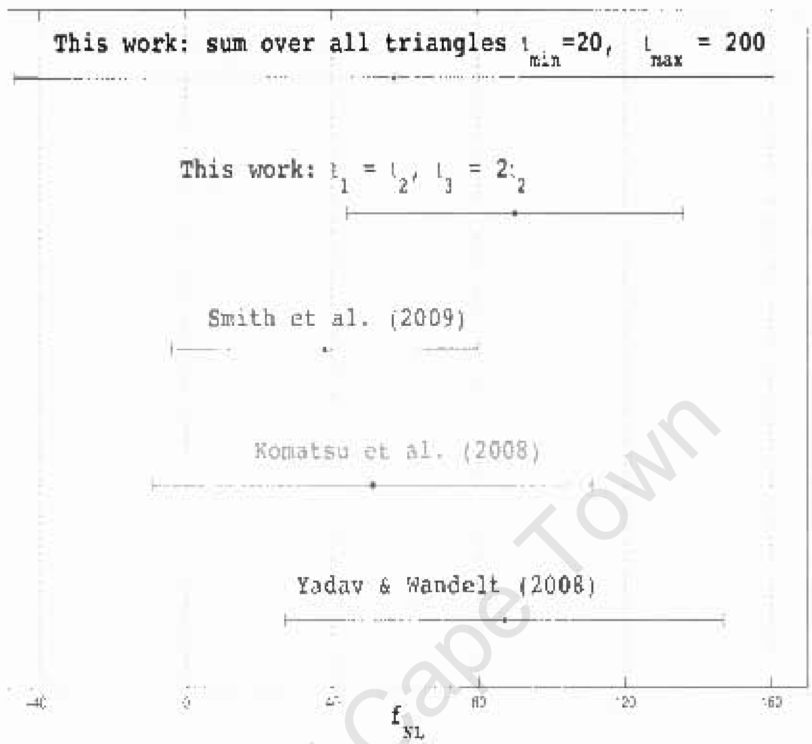

FIGURE 4.6: Comparison of the the f_{NL} constraints from our analysis and the latest WMAP constraints.

Triangle type	$\ell_{\max} = 100$	$\ell_{\max} = 200$	$\ell_{\max} = 300$	$\ell_{\max} = 400$
$\ell_1 = \ell_2 = \ell_3$	-179 ± 798	-272 ± 778	-264 ± 775	-277 ± 774
$\ell_1 = \ell_2$; $\ell_3 = 2\ell_1$	72 ± 27	90 ± 23	96 ± 23	100 ± 23
ℓ_1; $\ell_2 = 2\ell_1$; $\ell_3 = 3\ell_2$	-810 ± 930	-449 ± 705	-336 ± 689	-357 ± 687
ℓ_1; $\ell_2 = 4\ell_1$; $\ell_3 = 5\ell_1$	19 ± 90	-1011 ± 592	-1127 ± 563	-1108 ± 559
ℓ_1; $\ell_2 = 5\ell_1$; $\ell_3 = 6\ell_1$		3 ± 30	7 ± 24	4 ± 23

TABLE 4.5: This table illustrates the effect of $\ell_{\max}$ on the constraint of f_{NL} in the first redshift bin, $0.45 \leq z < 0.5$. In our analysis we use $\ell_{\max} = 200$, the limit of the quasi-linear region for the MegaZ-LRG mean redshift, $z = 0.5$

University of Cape Town

4.3 Implications and Future Work

Taken at face value, the result (4.14) suggests a detection of primordial non-Gaussianity and $f_{NL} > 0$ at more than $4-\sigma$, which would be the strongest detection so far and would put severe constraints on models of inflation. We have ruled out the obvious possible sources of error in obtaining these results by rigorously comparing our code against a range of tests, many of them discussed in the appendices. We are condent, therefore, that our data analysis results are robust, within the limitations of our analysis.

Probably the three biggest limitations of our analysis are the fact that we do not marginalise over the bias parameters, we use the theoretical estimates for the error on the bispectrum and we have not removed the non-Gaussianity that will inevitably be produced by nonlinear gravitational collapse. Let us discuss these in turn.

If we marginalised over the bias parameters it would somewhat reduce the statistical significance of our results by increasing the error bars associated with f_{NL}. In the case of local non-Gaussianity that we focus on here, this is expected to have a small impact (unlike the non-local case where the degeneracy is strong) as shown in Fig. (4.7) [40]. Marginalisation over bias parameters is an important issue left for future work.

Next consider the theoretical estimate, Eq. (2.33), for the error on the bispectrum. This may be a poor approximation for two reasons. Firstly we are dealing with a partial sky and one might worry that the theoretical prediction is bad. And secondly if the non-Gaussian signal in the data is significant, the theoretical estimate of the bispectrum co-variance will have an additional more complicated term and hence our estimate will be wrong. However, since we are expecting the departure from Gaussianity to be small, the theoretical estimate of the error we are using here is a good approximation [25, 71].

Next let us consider the non-Gaussianity induced by nonlinear collapse. This will mimic a non-zero f_{NL}, particularly for the equilateral configuration. We filtered for this contaminant however by limiting our analysis to relatively large angular scales, $\ell_{\max} = 200$, where the non-Gaussianities from nonlinear collapse should be negligible. We have seen from the above section that our our choice of the ℓ_{max}

University of Cape Town

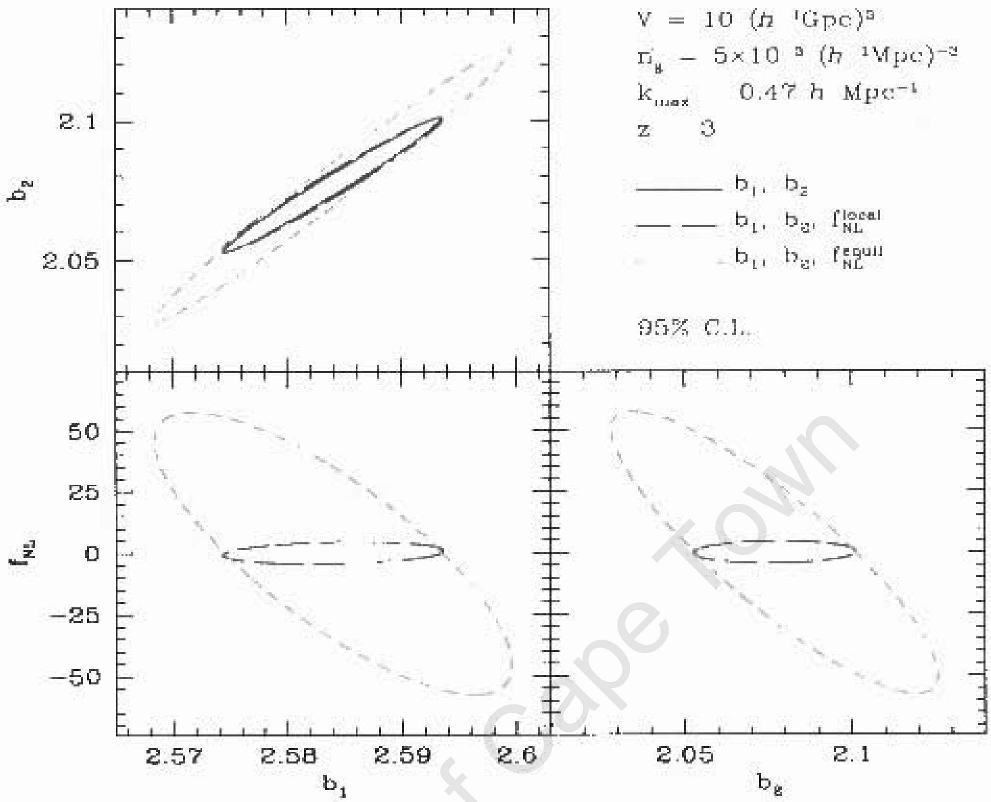

FIGURE 4.7: Degeneracy of the local and non-local (equilateral, denoted here as 'equil') f_{NL} with the linear and non-linear bias parameters. We see that the local type is uncorrelated with the bias parameters whereas the equilateral f_{NL} is very degenerate with both the linear and non-linear bias parameters [40]. Since we focus on squeezed configurations we argue that bias is less important for our results.

University of Cape Town

is conservative. Our result is not dominated by large ℓ and hence it excludes the possibility of the non-Gaussianity from nonlinear collapse.

Finally, there may be some unknown error or, more excitingly, our results may reect true non-Gaussianity in the large scale structure of the late universe. In this case what we need to understand and interpret in the context of inflation is what it means to have a positive signal for the type of triangular configurations for which we detected positive f_{NL}. One interesting although speculative possibility is that there may well be primordial non-Gaussianity but it may not be of the simple form parametrised by f_{NL}. We leave the investigation of this possibility for future work.

4.4 Conclusions

Using thoroughly-tested code we have computed the angular bispectrum of the full photometric MegaZ LRG catalog and undertaken parameter estimation to compute the best-fitting values of f_{NL} which parametrises primordial non-Gaussianity in the expression (4.5). We have found strong evidence in one triangular configuration for $f_{NL} > 0$ at nearly $4 - \sigma$ and other configurations that favour and disfavour $f_{NL} > 0$ by $2.5 - \sigma$. However, summing over all configurations produces a result consistent with Gaussianity and hence further work will be required to denitely settle the issue.

If confirmed, our results would have important implications for models of the early universe since the simplest models of inflation predict small non-Gaussianity, $|f_{NL}| \lesssim 1$, and hence would be ruled out, implying that more complex models of inflation, or new physics completely, are at work.

University of Cape Town

Appendix A

A.1 Test of the power spectrum and bispectrum equations

The aim of this appendix is to show that the angular power spectrum and bispectrum equations we used in the analysis of the MegaZ-LRG catalogue are valid in the weak non-linear regime. We illustrate this by recovering the fact that the bispectrum is zero for a Gaussian distribution and also since the power spectrum for a uniform random distribution is just the shot noise, we demonestrate that it is equal to zero when the shot noise is subtracted.

A.1.1 Uniform distribution - with sky cut

For the partial sky, we have chosen the region $105 < RA < 270, -10 < Dec < +70$, since this is approximately the Sloan region we will be analyzing with the real survey. Since the window function mixes the different multipoles, we need to incorporate this effect in the angular power spectrum and bispectrum. Hence the final equation that we need to evaluate are:

$$A_{lm} = \sum_{\theta,\phi} Y_{lm}(\theta,\phi) - \sigma_0 I_{lm}. \tag{A.1}$$

$$C_l = \frac{1}{\sigma_0^2 f_{\rm sky}} \left[\frac{\sum_m |A_{lm}|^2}{J_{lm}} - \sigma_0\right] \tag{A.2}$$

$$B_{l_1 l_2 l_3} = \frac{1}{\sigma_0^3 f_{\rm sky}} \left[\sum_m A_{l_1 m_1} A_{l_2 m_2} A_{l_3 m_3} - K_{l_1,l_2,l_3}\sigma_0\right] \tag{A.3}$$

University of Cape Town

where $I_{l,m}$, $J_{l,m}$ and K_{l_1,l_2,l_3} are

$$I_{l,m} = \int_{\Delta\Omega} Y^*_{l,m} d\Omega \tag{A.4}$$

$$J_{l,m} = \int_{\Delta,\Omega} |Y_{l,m}|^2 d\Omega \tag{A.5}$$

$$K_{l_1,l_2,l_3} = \sqrt{\frac{(2l_1+1)(2l_2+1)(2l_3+1)}{4\pi}} \begin{pmatrix} l_1 & l_2 & l_3 \\ 0 & 0 & 0 \end{pmatrix}. \tag{A.6}$$

The second terms in the right hand side of Eq. (A.2) and Eq. (A.3) are the contribution of the shot noise to the power spectrum and bispectrum. The factors $1/\sigma_0^2$ and $1/\sigma_0^3$ in these equations are because we are working using the over density field

$$\delta = \frac{\rho - \bar{\rho}}{\bar{\rho}}.$$

The $1/f_{\rm sky}$ factor controls the partial sky bias in estimating the power spectrum and the bispectrum. We evaluate the integrals in Eq. (A.4) and Eq. (A.5) using Monte Carlo integration.

When evaluating the power spectrum and bispectrum error bars one has to take into account the correlations between adjacent multipoles caused by the presence of the sky cut. Correlation between adjacent multipoles can also be caused by a non-smooth window function. In order to use the χ^2 statistics therefore, one needs to compute the full co-variance matrix that includes all sources of correlations. However since this is time-consuming we prefer to bin up the measurements in bands, average over $\Delta\ell$, so as we can treat each bins as independent. The size of $\Delta\ell$ which result in independent bands can be estimated by calculating the mixing matrix $R_{l,l'}$, which given in Eq.(11) of Blake et al. [54]. As shown in [54] binning in bands of $\Delta\ell = 10$ results in less than 10% correlation between adjacent bands (see Fig. 3.7). Hence for our analysis we took $\Delta\ell = 10$. The modified equations of the power spectrum and bispectrum errors in the case of the partial sky is then given by [57]

$$\sigma(C_l) = \frac{1}{\sqrt{\Delta_l f_{\rm sky}(l+0.5)}} \frac{1}{\sigma_0} \tag{A.7}$$

$$\sigma(B_{l_1 l_2 l_3}) = \sqrt{f_{\rm sky}(C_{l_1} + \frac{1}{\sigma_0})(C_{l_2} + \frac{1}{\sigma_0})(C_{l_3} + \frac{1}{\sigma_0})\Delta_{l_1,l_2,l_3}} \tag{A.8}$$

The $f_{\rm sky}$ factor comes to our equations due to the presence of the sky cut [24].

University of Cape Town

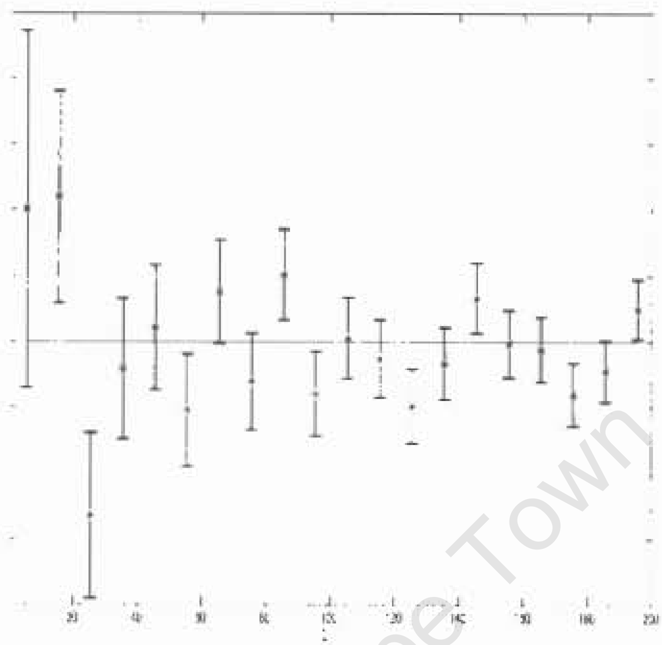

FIGURE A.1: Angular power spectrum of 10^5 points uniformly distributed over $105 < RA < 270, -10 < Dec < +70$, Sloan-like sky region. The red line is the theoretical power spectrum when the shot noise is subtracted, i.e zero.

For the real data, we will want to evaluate the power spectrum or the bispectrum for multipoles up to $\ell_{max} = 300$, because this is roughly the extent of the linear regime for the MegaZ catalogue mean redshift.

University of Cape Town

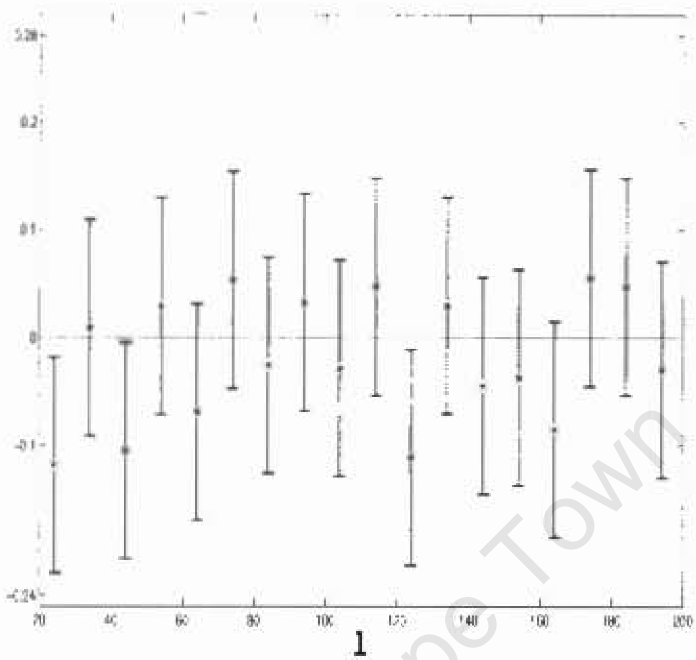

FIGURE A.2: Equilateral triangle ($\ell_1 = \ell_2 = \ell_3$) angular bispectrum of 10^5 uniformly distributed points over $105 < RA < 270, -10 < Dec < +70$, Sloan like sky region. The red line is the theoretical bispectrum, which is zero.

A.2 f_{NL} estimate from a Uniform distribution

To estimate the f_{NL} from a uniform random distribution, we follow the same procedure as described in section 4.2. The necessary steps involved towards implementing this is as follows.

1. Compute the bispectrum and its associated error bar for the uniform random distribution as described in the previous section.

2. Compute the theoretical bispectrum given by Eq. (4.11).

3. Compute the χ^2 over a grid of f_{NL}. The best-fitting f_{NL} corresponds to the f_{NL} that yields the minimum χ^2.

4. Given that the χ^2 is quadratic in f_{NL}, the 1,2, and 3 - σ confidence limits correspond to the values of f_{NL} for which the χ^2 is 1,4 and 9 larger than the minimum value, respectively.

University of Cape Town

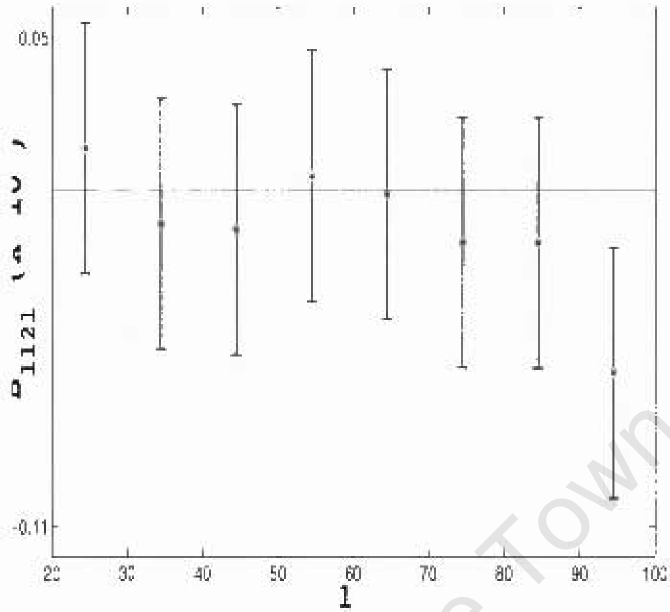

FIGURE A.3: Degenerate triangle ($\ell_1 = \ell_2, \ell_3 = 2\ell_1$) angular bispectrum of 10^5 uniformly distributed points over $105 < RA < 270, -10 < Dec < +70$, Sloan-like sky region. The red line is the theoretical bispectrum, which vanishes for a uniform distribution. This shows that our code does not introduce spurious non-Gaussian signals.

Following these steps for 10^5 points uniformly distributed over the SDSS MegaZ-LRG sky, we recovered that the f_{NL} is statistically consistent with zero for all the triangular configurations. Fig. (A.4) shows the equilateral ($\ell_1 = \ell_2 = \ell_3$) and degenerate ($\ell_1 - \ell_2, \ell_3 - \ell_2$) triangle bispectrum of the uniformly distributed points together with the best fitting theoretical bispectrum. In Table (A.1) we provide the best fitting f_{NL} value and the associated 1-σ error bar. We also recovered a vanishing primordial non-Gaussianity, $f_{NL} = 4 \pm 29$ with 68% CL, when we average over all possible triangular configurations for a uniform distribution.

The tests presented in this appendix show that our code does not introduce any spurious non-Gaussian signals, whether at the level of estimating the bispectrum or in the estimation of f_{NL}.

University of Cape Town

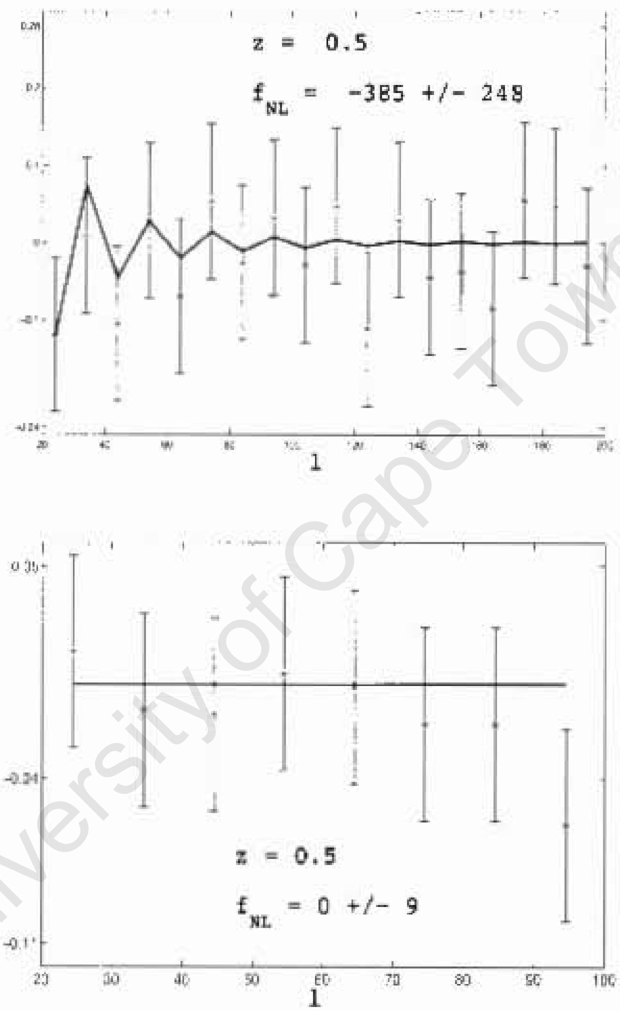

FIGURE A.4: The bispectrum of 10^5 points distributed uniformly over $105 < RA < 270, -10 < Dec < +70$ together with the theoretical bispectrum assuming non-zero primordial non-Gaussianity (the solid curve). The figures are the bispectrum for $\ell_1 = \ell_2 = \ell_3$ (top), $\ell_1 = \ell_2, \ell_3 = 2\ell_2$ (bottom) triangular configurations. The theoretical curve is evaluated at $z = 0.45$. The best fitting value of the f_{NL} is consistent with zero, as it is expected.

University of Cape Town

Triangle type	f_{NL} *with* 1σ *error*	*Min* χ^2	*Number of* σ *away from* $f_{NL} = 0$
$\ell_1 = \ell_2 = \ell_3$	-385 ± 248	4.4	$1.6\ \sigma$
$\ell_1 = \ell_2;\ \ell_3 = 2\ell_1$	0 ± 9	2.8	$0.1\ \sigma$
$\ell_1;\ \ell_2 = 2\ell_1;\ \ell_3 = 3\ell_2$	250 ± 326	2.3	$0.8\ \sigma$
$\ell_1;\ \ell_2 = 4\ell_1;\ \ell_3 = 5\ell_1$	-311 ± 399	0.1	$0.8\ \sigma$
$\ell_1;\ \ell_2 = 5\ell_1;\ \ell_3 = 6\ell_1$	2 ± 23	0.0	$0.1\ \sigma$

TABLE A.1: The constraint on f_{NL} from 10^5 points distributed uniformly over $105 < RA < 270, -10 < Dec < +70$. The minimum and maximum ℓ's considered here are $\ell_{\min} = 20$ and $\ell_{\max} = 200$.

University of Cape Town

Bibliography

[1] Weinberg, S., *Gravitation and cosmology: principles and applications of the general theory of relativity* (John Wiley & Sons, Inc. Press, 1972).

[2] Dodelson, S., *Modern Cosmology* (Cambridge University Press, 1998).

[3] Liddle, A., *An Introduction to Modern Cosmology* (John Wiley & Sons, Inc. Press, 2003).

[4] Eriksen, H. K., Banday, A. J., Górski, K. M., *et al.*, ApJ **660**, L81 (2007), `arXiv:astro-ph/0701089`.

[5] Vielva, P., Wiaux, Y., Martínez-González, E., *et al.*, MNRAS **381**, 932 (2007), `0704.3736`.

[6] Riess, A. G., Filippenko, A. V., Challis, P., *et al.*, ApJ **116**, 1009 (1998), `arXiv:astro-ph/9805201`.

[7] Perlmutter, S., Aldering, G., Goldhaber, G., *et al.*, ApJ **517**, 565 (1999), `arXiv:astro-ph/9812133`.

[8] Andrew R. Liddle, D. H. L., *Cosmological Inflation And Large-Scale Structure* (Cambridge University Press, 2000).

[9] Bassett, B. A., Tsujikawa, S., and Wands, D., Reviews of Modern Physics **78**, 537 (2006), `arXiv:astro-ph/0507632`.

[10] Blake, C. and Bridle, S., MNRAS **363**, 1329 (2005), `arXiv:astro-ph/0411713`.

[11] Penzias, A. A. and Wilson, R. W., ApJ **142**, 419 (1965).

[12] Eisenstein, D. J. and Hu, W., ApJ **511**, 5 (1999), `arXiv:astro-ph/9710252`.

[13] Sachs, R. K. and Wolfe, A. M., ApJ **147**, 73 (1967).

University of Cape Town

[14] Silk, J., Nature **215**, 1155 (1967).

[15] Smoot, G. F., Bennett, C. L., Kogut, A., *et al.*, ApJ **396**, L1 (1992).

[16] Nolta, M. R., Dunkley, J., Hill, R. S., *et al.*, ArXiv e-prints **803** (2008), `0803.0593`.

[17] Hinshaw, G., Nolta, M. R., Bennett, C. L., *et al.*, ApJS **170**, 288 (2007), `arXiv:astro-ph/0603451`.

[18] Komatsu, E., Dunkley, J., Nolta, M. R., *et al.*, ArXiv e-prints **803** (2008), `0803.0547`.

[19] Yadav, A. P. S. and Wandelt, B. D., Physical Review Letters **100**, 181301 (2008), `arXiv:0712.1148`.

[20] Smith, K. M., Senatore, L., and Zaldarriaga, M., ArXiv e-prints (2009), `0901.2572`.

[21] Slosar, A., Hirata, C., Seljak, U., *et al.*, Journal of Cosmology and Astro-Particle Physics **8**, 31 (2008), `0805.3580`.

[22] Afshordi, N. and Tolley, A. J., Phys. Rev. D. **78**, 123507 (2008), `0806.1046`.

[23] Spergel, D. N. and Goldberg, D. M., Phys. Rev. D **59**, 103001 (1999).

[24] Komatsu, E. and Spergel, D. N., in *The Ninth Marcel Grossmann Meeting*, edited by Gurzadyan, V. G., Jantzen, R. T., and Ruffini, R. (2002), pp. 2009–2010.

[25] Santos, M. G., Heavens, A., Balbi, A., *et al.*, MNRAS **341**, 623 (2003), `arXiv:astro-ph/0211123`.

[26] Babich, D., Creminelli, P., and Zaldarriaga, M., Journal of Cosmology and Astro-Particle Physics **8**, 9 (2004), `arXiv:astro-ph/0405356`.

[27] Byrnes, C. T., Sasaki, M., and Wands, D., Phys. Rev. D. **74**, 123519 (2006), `arXiv:astro-ph/0611075`.

[28] Kogo, N. and Komatsu, E., Phys. Rev. D. **73**, 083007 (2006), `arXiv:astro-ph/0602099`.

[29] Arroja, F. and Koyama, K., Phys. Rev. D. **77**, 083517 (2008), `arXiv:0802.1167`.

University of Cape Town

[30] Hikage, C., Coles, P., Grossi, M., *et al.*, MNRAS **385**, 1613 (2008), arXiv:0711.3603.

[31] Hikage, C., Matsubara, T., Coles, P., *et al.*, ArXiv e-prints **802** (2008), 0802.3677.

[32] Aghanim, N., Kunz, M., Castro, P. G., *et al.*, A&A **406**, 797 (2003), arXiv:astro-ph/0301220.

[33] Guth, A. H., Phys. Rev. D. **23**, 347 (1981).

[34] Starobinskij, A. A., Physics Letters B **91**, 99 (1980).

[35] Linde, A. D., Physics Letters B **108**, 389 (1982).

[36] Tsujikawa, S., ArXiv High Energy Physics - Phenomenology e-prints (2003), arXiv:hep-ph/0304257.

[37] Langlois, D., ArXiv e-prints (2008), 0811.4329.

[38] Bartolo, N., Matarrese, S., and Riotto, A., Journal of Cosmology and Astro-Particle Physics **1**, 3 (2004), arXiv:astro-ph/0309692.

[39] Bartolo, N., Komatsu, E., Matarrese, S., *et al.*, Physics Reports **402**, 103 (2004), arXiv:astro-ph/0406398.

[40] Sefusatti, E. and Komatsu, E., Phys. Rev. D. **76**, 083004 (2007), arXiv:0705.0343.

[41] Creminelli, P., Senatore, L., and Zaldarriaga, M., Journal of Cosmology and Astro-Particle Physics **3**, 19 (2007), arXiv:astro-ph/0606001.

[42] Bean, R., Chung, D. J. H., and Geshnizjani, G., Phys. Rev. D. **78**, 023517 (2008), 0801.0742.

[43] Bartolo, N., Matarrese, S., and Riotto, A., Journal of High Energy Physics **4**, 6 (2004), arXiv:astro-ph/0308088.

[44] Lyth, D. H. and Wands, D., Phys. Rev. D. **68**, 103516 (2003), arXiv:astro-ph/0306500.

[45] Bartolo, N., Matarrese, S., and Riotto, A., Physical Review D **69**, 043503 (2004), URL http://www.citebase.org/abstract?id=oai:arXiv.org:hep-ph/0309033.

University of Cape Town

[46] Peacock, H. A., *Cosmological Physics* (Cambridge University Press, 1998).

[47] Eisenstein, D. J., ArXiv Astrophysics e-prints (1997), `arXiv:astro-ph/9709054`.

[48] Scoccimarro, R., Sefusatti, E., and Zaldarriaga, M., Phys. Rev. D. **69**, 103513 (2004), `arXiv:astro-ph/0312286`.

[49] Coles, P., *Statistical properties of Cosmological fluctuations* (2002), `arXiv:astro-ph/0209590v1`.

[50] Matarrese, S., Verde, L., and Heavens, A. F., MNRAS **290**, 651 (1997), `arXiv:astro-ph/9706059`.

[51] Verde, L., Heavens, A. F., and Matarrese, S., MNRAS **318**, 584 (2000), `arXiv:astro-ph/0002240`.

[52] Verde, L., in *The Onset of Nonlinearity in Cosmology*, edited by Fry, J. N., Buchler, J. R., and Kandrup, H. (2001), vol. 927 of *New York Academy Sciences Annals*, pp. 54–+.

[53] M.S Bartlett, R. M. and Terrence, J. S., *Face Recognition by Independent Component Analysis* (2001).

[54] Blake, C., Collister, A., Bridle, S., *et al.*, MNRAS **374**, 1527 (2007), `arXiv:astro-ph/0605303`.

[55] Baldi, D., P. Marinucci, Annals of Statistics 2004, Vol. 32, No. 3, 1261-1288 (2006), `arXiv:math/0406526v1`.

[56] Baldi, D., P. Marinucci, Statist. Probab. Letters 77, 490–496 (2007) (2007), `arXiv:math/0606709`.

[57] Dolney, D., Jain, B., and Takada, M., MNRAS **366**, 884 (2006), `arXiv:astro-ph/0409445`.

[58] Collister, A., Lahav, O., Blake, C., *et al.*, MNRAS **375**, 68 (2007), `arXiv:astro-ph/0607630`.

[59] Eisenstein, D., Annis, J., Gunn, J., *et al.*, Astrophysical Journal **122**, 2267 (2001), `arXiv:astro-ph/0108153`.

University of Cape Town

[60] Wake, D. A., Sheth, R. K., Nichol, R. C., *et al.*, MNRAS **387**, 1045 (2008), arXiv:0802.4288.

[61] Gunn, J. E., in *Bulletin of the American Astronomical Society* (1995), vol. 27 of *Bulletin of the American Astronomical Society*, pp. 875–+.

[62] Fukugita, M., Ichikawa, T., Gunn, J. E., *et al.*, ApJ **111**, 1748 (1996).

[63] Uomoto, A., Smee, S., Rockosi, C., *et al.*, in *Bulletin of the American Astronomical Society* (1999), vol. 31 of *Bulletin of the American Astronomical Society*, pp. 1501–+.

[64] Abazajian, K. and Sloan Digital Sky Survey, f. t., ArXiv e-prints (2008), 0812.0649.

[65] Górski, K. M., Hivon, E., Banday, A. J., *et al.*, ApJ **622**, 759 (2005), arXiv:astro-ph/0409513.

[66] Scranton, R., Connolly, A. J., Szalay, A. S., *et al.*, ArXiv Astrophysics e-prints (2005), arXiv:astro-ph/0508564.

[67] Collister, A. A. and Lahav, O., PASP **116**, 345 (2004), arXiv:astro-ph/0311058.

[68] Padmanabhan, N., Schlegel, D. J., Seljak, U., *et al.*, MNRAS **378**, 852 (2007), arXiv:astro-ph/0605302.

[69] Simon, P., A&A **473**, 711 (2007), arXiv:astro-ph/0609165.

[70] LoVerde, M. and Afshordi, N., ArXiv e-prints (2008), 0809.5112.

[71] Gangui, A. and Martin, J., MNRAS **313**, 323 (2000), arXiv:astro-ph/9908009.

University of Cape Town